

1
2 **Enhancing Long-Term Trend Simulation of Global**
3 **Tropospheric OH and Its Drivers from 2005-2019: A**
4 **Synergistic Integration of Model Simulations and Satellite**
5 **Observations**

6
7 **Amir H. Souri^{1,2*}, Bryan N. Duncan¹, Sarah A. Strode^{1,2}, Daniel C. Anderson^{1,3}, Michael E. Manyin^{1,4},**
8 **Junhua Liu^{1,2}, Luke D. Oman¹, Zhen Zhang^{5,6}, and Brad Weir^{2,7}**

9
10 ¹Atmospheric Chemistry and Dynamics Laboratory, NASA Goddard Space Flight Center (GSFC),
11 Greenbelt, MD, USA

12 ²GESTAR II, Morgan State University, Baltimore, MD, USA

13 ³GESTAR II, University of Maryland Baltimore County, Baltimore, MD, USA

14 ⁴Science Systems and Applications, Inc., Lanham, MD, USA

15 ⁵National Tibetan Plateau Data Center (TPDC), State Key Laboratory of Tibetan Plateau Earth System,
16 Environment and Resource (TPESER), Institute of Tibetan Plateau Research, Chinese Academy of
17 Sciences, Beijing, China

18 ⁶Earth System Science Interdisciplinary Center, University of Maryland, College Park, MD, USA

19 ⁷NASA Global Modeling and Assimilation Office (GMAO), Goddard Space Flight Center, Greenbelt,
20 MD, USA

21
22 * Corresponding author: a.souri@nasa.gov
23

24 Abstract

25 The tropospheric hydroxyl radical (TOH) is a key player in regulating oxidation of various compounds in
26 Earth's atmosphere. Despite its pivotal role, the spatiotemporal distributions of OH are poorly constrained.
27 Past modeling studies suggest that the main drivers of OH, including NO₂, tropospheric ozone (TO₃), and
28 H₂O(v), have increased TOH globally. However, these findings often offer a global average and may not
29 include more recent changes in diverse compounds emitted on various spatiotemporal scales. Here, we aim
30 to deepen our understanding of global TOH trends for more recent years (2005-2019) at 1×1 degrees. To
31 achieve this, we use satellite observations of HCHO and NO₂ to constrain simulated TOH using a technique
32 based on a Bayesian data fusion method, alongside a machine learning module named ECCOH, which is
33 integrated into NASA's GEOS global model. This innovative module helps efficiently predict the
34 convoluted response of TOH to its drivers/proxies in a statistical way. Aura Ozone Monitoring Instrument
35 (OMI) NO₂ observations suggest that the simulation has high biases over biomass burning activities in
36 Africa and Eastern Europe, resulting in overestimation of up to 20% in TOH, regionally. OMI HCHO
37 primarily impacts oceans where TOH linearly correlates with this proxy. Five key parameters including
38 TO₃, H₂O(v), NO₂, HCHO, and stratospheric ozone can collectively explain 65% of variance in TOH trends.
39 The overall trend of TOH influenced by NO₂ remains positive, but it varies greatly because of the
40 differences in the signs of anthropogenic emissions. Over oceans, TOH trends are primarily positive in the
41 northern hemisphere, resulting from the upward trends in HCHO, TO₃, and H₂O(v). Using the present
42 framework, we can tap the power of satellites to quickly gain a deeper understanding of simulated TOH
43 trends and biases.

44 1. Introduction

45 The hydroxyl radical (OH) regulates the lifetimes of a vast number of key atmospheric compounds,
46 such as sulfur dioxide (SO₂), nitrogen dioxide (NO₂), volatile organic compounds (VOCs), carbon
47 monoxide (CO), and methane (CH₄). Despite its outsized importance for atmospheric chemistry and
48 climate, our knowledge on both the abundance and long-term trends of OH is limited due to its sparse
49 observations, manifesting in large discrepancies between simulated OH among global models (e.g., Naik
50 et al., 2013; Zhao et al., 2019; Murray et al., 2021; Fiore et al., 2024). Particularly, these discrepancies can
51 introduce large uncertainties when it comes to precisely representing methane (Holmes et al., 2013; Nguyen
52 et al., 2020), a potent greenhouse gas. Consequently, to understand the potential impact of this warming
53 agent on climate shifts and extreme weather events, it is essential to accurately simulate methane
54 concentration within a coupled climate model, such as the NASA's Goddard Earth Observing System
55 (GEOS) model (Molod et al., 2015; Nielsen et al., 2017), which requires reasonable representation of its
56 major sink – reaction with OH.

57 Despite the challenges posed by OH's short lifespan of less than two seconds, low-pressure laser-
58 induced fluorescence spectroscopy has proven invaluable in measuring OH for over twenty airborne field
59 campaigns (Miller and Brune, 2020). These datasets have been instrumental in verifying the efficacy of
60 chemical mechanisms involving varying reaction rate coefficients and aerosol heterogeneous chemistry
61 (Brune et al., 2019; Miller and Brune, 2020; Brune et al., 2022), understanding urban air quality (Brune et
62 al., 2022; Sourì et al., 2023), as well as identifying potential sources of HO_x (OH+HO₂) that may have been
63 hampered due to instrument detection limits and/or unmeasured compounds (e.g., Ren et al., 2008).
64 However, while these observations offer valuable insights, they are limited in time and space and cannot
65 provide a full picture of tropospheric OH abundance.

66 There are several approaches that have been employed to constrain OH needed for replicating
67 observed values of a tracer whose primary sink is OH and its sources are relatively well known. One notable
68 method is methyl chloroform (MCF) inversion (Patra et al., 2014; Turner et al., 2017; Rigby et al., 2017;

69 Naus et al., 2019). However, this method only provides hemispheric-average OH and is thus insufficient to
70 resolve the spatial distribution of OH.

71 A more sophisticated approach to constraining OH is to incorporate well-characterized satellite
72 observations of factors known to influence OH, such as NO₂, CO, ozone, and formaldehyde (HCHO), into
73 a chemical transport model using inverse modeling and/or chemical data assimilation methods (Sandu and
74 Chai, 2011; Bocquet et al., 2015). This method offers a crucial advantage in that it accounts for the
75 interconnectedness of various chemical and physical processes within model increments. For example,
76 adjustments to NO_x levels will impact nitrate and ozone concentrations, which in turn affect the HO₂ uptake
77 through aerosols, OH, and radiation, reciprocally leading to a more accurate representation of NO_x. Several
78 studies have used subsets of satellite observations to improve HO_x and ozone chemistry, with Miyazaki et
79 al. (2020) using a diverse range of observations, including CO, NO₂, O₃, and nitric acid (HNO₃), to improve
80 model predictions using a local ensemble Kalman filter. The incorporation of these observations led to a
81 reduction in the asymmetric OH ratio between the northern and southern hemispheres, aligning better with
82 MCF results (Patra et al., 2014). Similarly, Souri et al. (2020a) leveraged well-characterized observations
83 of HCHO and NO₂ to improve ozone chemistry over East Asia using non-linear analytical Bayesian
84 inversion, observing significant changes in OH levels after adjusting biogenic VOC in southeast Asia.
85 While incorporating these observations into atmospheric models offers a comprehensive way to gain
86 insights into spatiotemporal OH variability, it is complicated by several layers of complexity, such as
87 unidentified satellite biases, unresolved scales in satellite observations, and errors in models including
88 transport, chemical mechanisms, vertical diffusion, and depositions rates. Understanding how these errors
89 could cloud the realistic determination of OH requires running constrained models under various
90 realizations, which is computationally prohibitive.

91 Researchers have developed OH predictors based on a set of key parameters, offering reasonable
92 spatial and temporal coverage without compromising computational efficiency (Spivakovsky et al., 2000;
93 Duncan et al., 2000; Elshorbany et al., 2016; Nicely et al., 2018; Wolfe et al., 2019; Nicely et al., 2020;
94 Anderson et al., 2022, Zhu et al., 2022; Anderson et al., 2023; Baublitz et al., 2023). These studies fall into
95 four categories, the first of which uses box model photochemical simulations to predict OH levels under a
96 steady-state assumption, using a blend of pre-modeled fields and various observations influencing OH
97 (Spivakovsky et al., 2000; Nicely et al., 2018). The second group uses proxy observations (e.g., HCHO or
98 water, H₂O) of OH in remote areas (Wolfe et al., 2019; Baublitz et al., 2023). The third group employs
99 high-order polynomials to establish an empirical relationship between OH and different parameters,
100 avoiding the need to solve numerous differential equations in chemical mechanisms (Duncan et al., 2000;
101 Elshorbany et al., 2016). Finally, the fourth group leverages powerful machine learning algorithms to
102 encapsulate the complexities between OH and its key influencers to efficiently predict OH using a
103 comprehensive dataset which is easily exchangeable between models (Nicely et al., 2020; Anderson et al.,
104 2022; Zhu et al., 2022; Anderson et al., 2023).

105 In this work, we demonstrate the potential of a new approach to constrain simulated OH that uses
106 satellite observations to adjust the input parameters to an improved parameterization of OH (Anderson et
107 al., 2022), within the Efficient CH₄-CO-OH (ECCOH) (pronounced “echo”) configuration (Elshorbany et
108 al., 2016) of NASA’s GEOS model. We use the Modern-Era Retrospective analysis for Research and
109 Applications, Version 2 (MERRA2) reanalysis data (Molod et al., 2015) to constrain meteorology and
110 adjust two critical OH inputs using the latest Aura Ozone Monitoring Instrument (OMI) NO₂ and HCHO
111 retrievals (Lamsal et al., 2021; Nowlan et al., 2023) from 2005-2019 worldwide. Through conducting a
112 range of experiments, we determine the extent to which leveraging OMI NO₂ and HCHO observations can
113 enhance current representations of these two species derived from a global model simulation, MERRA2-
114 GMI (hereafter M2GMI) (Strode et al., 2019), so that we can achieve more accurate portrayals of OH
115 abundance and its long-term trends. Ultimately, we deconvolve the intricate OH trend maps into five critical
116 parameters using various modeling experiments, including tropospheric ozone, stratospheric ozone, NO₂,
117 HCHO, and H₂O.

118 Our paper is structured into several sections. In sections 2.1 to 2.3, we discuss the model
119 configurations, Bayesian data fusion algorithm, and satellite observations used. In section 2.4, we outline

120 our modeling experiments, which aim to uncover the impact of various key OH inputs on its trends and
121 assess the effect of OMI adjustments. In section 3.1, we examine the discrepancies between our prior
122 knowledge from M2GMI and OMI observations and demonstrate how the data fusion can mitigate these
123 differences. In section 3.2, we delve into the effect of OMI adjustments to NO₂ and HCHO on tropospheric
124 OH (TOH) magnitudes across the globe. In section 3.3, we focus on understanding the long-term effect of
125 a set of key inputs on OH and how well they can replicate our most dynamic representation of TOH. In
126 Section 4, we summarize the potential of using satellite observations in conjunction with well-characterized
127 models to identify biases and long-term trends in TOH and discuss the limitations of our current analysis
128 and potential paths forward.

129 **2. Models, Methods, and Measurements**

130 *2.1. Models*

131 *2.1.1. GEOS*

132 The GEOS model (Molod et al., 2015; Nielsen et al., 2017) simulates global weather with
133 1° longitude × 1° latitude spatial resolution. The model follows 72 hybrid sigma values ranging
134 from the surface to 0.01 hPa. We employ a cumulus parameterization to consider deep convection
135 (Moorthi and Suarez, 1992). Cloud microphysics is determined by a single-moment
136 parameterization based on Bacmeister et al. (2006). We activate the "replay" option (Orbe et al.,
137 2017) to constrain several meteorological variables using the MERRA-2. Sea surface temperatures
138 and ice content are pre-described from various observations (Nielsen et al., 2017; Reynolds et al.,
139 2007). Speciated aerosol concentrations and their optical properties are simulated by the GOCART
140 model (Chin et al., 2002) within GEOS. The rapid radiative transfer model for GCMs (RRTMG)
141 resolves the long- and short-wave radiation imposed by GOCART-simulated aerosols, allowing for
142 the direct impact of aerosol on meteorology to be taken into consideration (Nielsen et al., 2017).
143 The period of simulation starts in 2005 and ends in 2020. Ten years before 2005 are considered for
144 the spin-up of meteorological, CO, and CH₄ fields.

145 *2.1.2. ECCOH*

146 A computationally-efficient module, named ECCOH was developed to simulate the
147 chemistry of the CH₄-CO-OH cycle in the GEOS-5 model framework (Elshorbany et al., 2016).
148 CO and CH₄ tracers are explicitly simulated and their emissions are discussed in Sections 2.1.2.1
149 and 2.1.2.2. A key component of ECCOH is the parameterization of tropospheric OH, which was
150 developed using a gradient boosted regression tree machine learning algorithm (Anderson et al.,
151 2022) and is a function of chemical, solar irradiance, and meteorological variables. The training
152 dataset of chemical and meteorological variables was a 40-year daily M2GMI model simulation
153 (Strode et al. 2019), which includes tropospheric chemistry involving 120 species and 400 reactions
154 with the GMI mechanism (Duncan et al., 2007a and the references therein) and uses MERRA-2
155 reanalysis to constrain transport and meteorology at 0.625×0.5 degrees.

156 We present the variables used as inputs to the parameterization of OH for this study in
157 Table 1. The daily archived chemical inputs are from the M2GMI simulation with several variables
158 being constrained with observations. For instance, both NO₂ and HCHO fields are corrected
159 whenever satellite observations are available as described in Section 2.2.1. We chose NO₂, an
160 observable compound from satellites and a reasonable proxy for NO_x that has been shown to affect
161 OH (e.g., Zhao et al., 2020; Anderson et al., 2022). HCHO is used as a proxy for VOC oxidation
162 via OH in remote oceanic regions (Wolfe et al., 2019).

163 There are also long-term satellite data records of other OH drivers, including water vapor
164 (e.g., Aqua AIRS) and total ozone column (e.g., Aura OMI), that we could also consider. However,
165 the GEOS MERRA-2 system already assimilates satellite datasets of water vapor and the M2GMI
166 simulation simulates well (i.e., <4%) the total ozone column as compared to observations (Figure
167 S1). The integrated water vapor columns from MERRA2 and microwave-based satellite
168 observations over-ocean also agree well (<5%), especially after 2000 when many satellite
169 observations have been used in the reanalysis data (Figure 3 in Bosilovich et al., 2017). Therefore,
170 the application of the "replay" mode constrains various meteorological fields, providing a more
171 realistic reconstruction of OH studied here.

172 Tropospheric ozone is another critical input to the parameterization of OH. Although we
173 will compare M2GMI tropospheric ozone with satellite observations to locate any differences,
174 reliable measurements of tropospheric ozone from satellites are lacking due to the limited
175 sensitivity of the retrievals to ozone in low altitudes. Therefore, our study refrains from imposing
176 any observational constraint on tropospheric ozone.

177 Throughout the paper, TOH is determined based on the methane-reaction-weighted OH
178 suggested by Lawrence et al. (2001).

179 *2.1.2.1. Monthly CO emissions*

180 We use a modified version of EDGAR (Emissions Database for Global
181 Atmospheric Research) v5.0 (Crippa et al., 2019), which is a comprehensive database that
182 provides estimates of sector-based CO emissions from human activities (i.e.,
183 anthropogenic) on a global scale. Previous studies (e.g., Zheng et al., 2019) suggested a
184 large underestimation of EDGAR CO emissions for India and China. Accordingly, we
185 scale up the residential and transportation emissions from China by a factor of 1.6, and the
186 residential emissions from India by a factor of 1.2 based on Zheng et al. (2019). The
187 emissions spanned the entirety of the study period, from 2005 until 2020, and were
188 prepared monthly at a spatial resolution of $0.1^\circ \times 0.1^\circ$. The daily biomass burning emissions
189 are CMIP6 emissions, which derived from on the Global Fire Emissions Database version
190 4 with small fires (GFED4s) (van Marle et al., 2017). To account for the chemical
191 production of CO from the oxidation of non-methane VOCs, we adopt the CO yield
192 estimates from Duncan et al. (2007b) (i.e., a molar yield of 20% from isoprene, 20% from
193 monoterpenes, 100% from methanol, 67% from acetone, 19% from anthropogenic VOC
194 emissions, and 11% from biomass burning VOC sources) and released these CO emissions
195 in the first vertical level of the model. With regards to the biogenic VOC emissions used
196 for the above CO production estimates, we use offline MEGAN calculations using a
197 GEOS-Chem (v13.2.0) run. CO production from CH₄ oxidation is calculated online for
198 each model box.

199 *2.1.2.2. Monthly CH₄ emissions*

200 In this study, several bottom-up CH₄ emissions related to anthropogenic, wetland,
201 natural, and biomass burning sources are used to simulate CH₄. The monthly-basis
202 anthropogenic sources are derived from EDGARv6 (Ferrario et al., 2021). The biomass
203 burning emissions come from the GFED4s. Because EDGARv6 accounts for agricultural
204 waste burning, we exclude this specific source from the GFED4. Following Strode et al.
205 (2020), we use modified monthly-basis natural emissions from ocean, termite, and mud
206 volcano emissions. Wetland emissions are derived from an improved dynamic wetland
207 emission framework at $0.5^\circ \times 0.5^\circ$ based on the TOPography-based hydrological model
208 (TOPMODEL) (Zhang et al., 2016; Zhang et al., 2023). A climatological sink of CH₄ from
209 soil uptake is subtracted from the total CH₄ emissions.

210
211
212

Table 1. The list of inputs used for the parametrization of OH.

Input Group	Variables (Directly Constrained)	Source	Temporal Resolution
Offline Chemical Species	NO ₂ , HCHO, O ₃ , isoprene, acetone, H ₂ O ₂ , propene, propane, methyl hydroperoxide, ethane, C4 and C5 alkanes, and stratospheric O ₃ columns	M2GMI (offline) (Strode et al. 2019)	Daily-averaged
Online Chemical Species	CO and CH ₄	GEOS (online)	Daily-averaged
Meteorological Fields	T, P, Qv , and cloud fraction	GEOS (online)	Daily-averaged
Optical Properties	Aerosol optical depth; ice crystal cloud optical depth; and water droplet cloud optical depth at above and below of a given model vertical layer.	GEOS (online)	Daily-averaged
Geographic Information	Latitude and solar zenith angle (SZA)	Calculated	Fixed for latitude, but daily for SZA based on local noontime
Surface Properties	Surface UV albedo	OMI LER climatology (Qin et al., 2019; Fasnacht et al., 2019)	Monthly (climatology)

213

214 2.2. Methods

215 2.2.1. Bayesian data fusion for NO₂ and HCHO fields using OMI retrievals

216 To improve the representation of M2GMI NO₂ and HCHO concentrations and their long-
217 term trends, which are used as input to the parameterization of OH in ECCOH, we scale their
218 columnar mass using Aura OMI observations of NO₂ and HCHO columns (described in Sections
219 2.3.1 and 2.3.2) using an offline version of the optimal interpolation (OI) method (Parish and
220 Derber, 1992; Jung et al., 2019) with an appropriate regularization. If we assume that the error
221 covariances of M2GMI columns and OMI ones follow a Gaussian distribution with zero means and
222 their relationships are linear, we can estimate new columns using Bayes' theorem (Rodgers, 2000):

$$\mathbf{X}_a = \mathbf{X}_b + \gamma \mathbf{B} \mathbf{H}^T (\gamma \mathbf{H} \mathbf{B} \mathbf{H}^T + \mathbf{E})^{-1} (\mathbf{Y} - \mathbf{H} \mathbf{X}_b) \quad (1)$$

223 where \mathbf{X}_b is the prior M2GMI columns (i.e., background), \mathbf{X}_a is the posterior M2GMI columns
224 (i.e., analysis), \mathbf{B} is the error covariance matrix of the a priori, \mathbf{E} is the sum squares of error
225 covariance matrix of the observations and the representation errors, \mathbf{Y} is the observations, and \mathbf{H} is
226 the observational operator which is equivalent to the identity matrix in our case. The instrument
227 error part of \mathbf{E} is populated by the average sum of precision error squares the satellite product

228 provides. We interpolate both \mathbf{E} and \mathbf{Y} into the M2GMI grid box using a mass-conserved linear
 229 barycentric interpolation method. In this method, both OMI observations and errors in the L2
 230 granules provided at their irregular grid have been projected into a common grid of 0.25×0.25
 231 degrees using Delaunay triangulation bi-linear interpolation. Subsequently, we convolve these re-
 232 gridded maps with a box filter whose kernel size is equivalent to the rounded fraction of M2GMI
 233 grid box size to the re-gridded OMI pixel size based on Souri et al. (2022). This interpolation method
 234 removes the spatial representation error resulting from the unresolved scales in M2GMI columns.
 235 Nonetheless, we did not take into account the errors of unresolved processes in M2GMI to augment
 236 to \mathbf{E} . The National Meteorological Center's (NMC) approach is a common technique for calculating
 237 \mathbf{B} in atmospheric models (Parish and Derber 1992; Souri et al., 2020b); however, due to computing
 238 constraints, rerunning the M2GMI model to create the 24-hour prediction segments needed in the
 239 NMC method was not possible. Instead, we initialize \mathbf{B} by setting it to 50% errors for NO_2 and
 240 HCHO, both of which are subject to regularization. γ is the regularization factor designed for
 241 achieving the best fit (minimum residuals between \mathbf{Y} and $\mathbf{H}\mathbf{X}_b$) while minimizing the effect of the
 242 noise in the observations (minimum variance in \mathbf{X}_a). To this end, we seek an optimal regularization
 243 factor based on finding the “knee point” in the curve of the incremental regularization factors
 244 (ranging from 0.1 to 10) and the degrees of freedom obtained from the optimization. The γ value
 245 is determined based on the average of all data points in a month and does not vary from pixel to
 246 pixel to ease the interpretation of the result. We did not account for the non-diagonal spatial
 247 correlations of \mathbf{B} , as it requires us to carry out the NMC method. We use the ratio of $\mathbf{X}_b/\mathbf{X}_a$
 248 to uniformly scale the three-dimensional concentrations of the target gas (i.e., NO_2 or HCHO). The
 249 error associated with the constrained M2GMI columns can be obtained via

$$\mathbf{S}_a = (\mathbf{I} - \gamma\mathbf{B}\mathbf{H}^T(\gamma\mathbf{H}\mathbf{B}\mathbf{H}^T + \mathbf{E})^{-1}\mathbf{H}) \times \gamma\mathbf{B} \quad (2)$$

250 The averaging kernels (AK) describe the amount of information gained from the observations are
 251 represented by

$$\text{AK} = \mathbf{I} - \frac{\mathbf{S}_a}{\mathbf{B}} \quad (3)$$

252 where \mathbf{I} is the identity matrix.

253 In our research, we have created an open-source Python package called OI-SAT-GMI
 254 (Souri, 2024), which possesses the ability to download and process OMI level 2 products, perform
 255 air mass factor (AMF) recalculation, and conduct mass-conserved interpolation, while also
 256 executing the OI algorithm.

257 In our approach, the adjustments are implemented to the M2GMI output (i.e., a data fusion
 258 approach instead of data assimilation one), thereby restricting the full use of improved NO_2 and
 259 HCHO representation for more accurate simulation of other chemical compounds impacted by NO_2
 260 and HCHO, including ozone (e.g., Souri et al., 2020a, 2021). Nevertheless, as the accuracy of NO_2
 261 concentrations can significantly impact OH and HCHO is strongly tied to VOC oxidation through
 262 OH in remote ocean areas (Wolfe et al., 2019), the adjustments are expected to be beneficial in
 263 achieving a more robust representation of OH.

264 2.2.2. Trend analysis

265 We determine a linear trend in a time series based on fitting the following equation
 266 accounting for a seasonal cycle and shorter frequencies in the observations:

$$\mathbf{y} = a_0 + a_1\mathbf{t} + \sum_{i=1}^3 a_{i+1}\cos 2\pi\omega_i(\mathbf{t} - \varphi_i) \quad (4)$$

267 The equation comprises several variables, including \mathbf{y} (data points) on monthly-basis, a_0 as the
 268 mean, a_1 as the linear trend, \mathbf{t} as time (fractional year), a_{i+1} , ω_i , and φ_i are the amplitude,
 269 frequency, and phase, respectively. We consider three harmonics ($\omega_i = 1,2,3$) to account for
 270 seasonal cycle ($\omega=1$) and higher frequencies. To assess the statistical significance of a trend, we

271 employ the Mann-Kendall test and consider a trend to be significant if the linear trend passes the
272 test at a 95% confidence level.

273 In the context of trend analysis, the careful examination of errors in observations (y) is a
274 critical aspect often overlooked. However, when the errors of observations are obtainable, such as
275 those obtained from satellites or constrained M2GMI fields, we determine the parameters by
276 applying a weighted estimation. This estimation is optimized using the Levenberg–Marquardt
277 algorithm (Marquardt et al., 1996) using *SciPy* open-source package. Considering the errors in the
278 observational data deemphasizes more uncertain data, resulting in a more realistic determination of
279 the linear trend.

280 2.2.3. OH response calculations

281 To elucidate the response of OH to different input parametrizations, such as NO₂, HCHO,
282 and O₃, we determine the semi-normalized sensitivities through a traditional finite difference
283 method:

$$SOH_i = \frac{[OH]_i^{110\%} - [OH]_i^{90\%}}{0.2} \quad (5)$$

284 where $[OH]_i^{110\%}$ and $[OH]_i^{90\%}$ are OH concentrations from perturbing input parameters (i) by 1.1
285 and 0.9 scaling factors in the ECCOH offline framework (Anderson et al., 2022). These calculations
286 are solely used to better understand why OH changes in a particular way relative to the changes in
287 its drivers. In our online modeling framework, OH is simultaneously affected by the dynamic
288 changes of various variables considered in the parametrization of OH.

289 It is crucial to acknowledge that ECCOH has established an implicit relationship between
290 OH and various input parameters statistically. These perturbations could involve a range of
291 physiochemical processes that are challenging to fully decipher. For example, the perturbation of
292 NO₂, acting as a surrogate of reactive nitrogen, involves chemical reactions that include reactive
293 nitrogen like NO+HO₂ and NO₂+OH, ozone formation, aerosol HO_x uptake, and radiation.
294 Nonetheless, it may not be feasible to understand the extent to which ECCOH has been considered.
295 Therefore, the presented perturbations in this work should be viewed qualitatively.

296 2.3. Measurements

297 2.3.1. OMI MINDS tropospheric NO₂ columns

298 To improve the representation of NO₂ fields used as input to the parameterization of OH,
299 we constrain the archived monthly fields with the most updated NASA standard tropospheric NO₂
300 product (v4.0; Lamsal et al., 2021) from Aura OMI. Aura has a local equatorial overpass time of
301 13:45 and nearly daily global coverage. This new OMI product version is improved in multiple
302 aspects as compared to the former products, including surface reflectance and cloud retrieval
303 (Lamsal et al., 2021).

304 The validation of OMI tropospheric NO₂ columns from the comparison to integrated
305 aircraft spirals obtained from diverse air quality campaigns revealed a good level of correlation
306 ($r > 0.7$) (Choi et al., 2020). However, large mean biases, approximately 40%, were observed. These
307 biases come from various sources, including systematic biases in prognostic data utilized in the
308 retrieval, biases inherent in the aircraft data, spatial representation errors (Judd et al., 2020; Souri
309 et al., 2022), and temporal representation errors. The spatial representation errors have been
310 recognized to notoriously drift the slopes from the unity line in validation studies (Souri et al.,
311 2022). Notably, Choi et al. (2020) achieved a substantial reduction in mean biases, decreasing from
312 40% to 16%, through the downscaling of OMI data into a finer resolution domain using a regional
313 chemical transport model. Likewise, Pinardi et al. (2020) reduced the biases between MAX-DOAS

314 and OMI NO₂ observations by considering a radial dilution factor to account for the mismatch
 315 scales between the satellite footprint and the pointwise observations. These studies showed that the
 316 true statistics describing OMI biases are unknown, but they tended to be milder than those derived
 317 from directly comparing large pixels with pointwise measurements. It is important to highlight that
 318 discrepancies between M2GMI and OMI NO₂ will surpass the reported biases, thereby
 319 underscoring the product’s reliability over diverse geographical regions.

320 The long-term trends of tropospheric NO₂ columns have undergone extensive comparative
 321 analyses with in-situ observations (Lamsal et al., 2015; Pinardi et al., 2020), regulatory inputs, and
 322 assessments of human and biomass burning activities (Duncan et al., 2016; Choi and Souri,
 323 2015a,b; Krotkov et al., 2016; Jin and Holloway, 2015; Souri et al., 2017; Rueter et al., 2014; de
 324 Foy et al., 2016; Hickman et al., 2021).

325 We prefer level 2 over level 3 products to enable the recalculation of AMFs with time-
 326 varying shape factors derived from the M2GMI simulation. We removed low-quality pixels using
 327 the main quality flag, cloud fraction >30%, terrain reflectivity >20%, and those pixels affected by
 328 the “row anomaly” complication. The data product, which has a spatial resolution ranging from
 329 ~13 km × 24 km (at nadir) to ~24 km × 160 km (at extremities of the scanline), were then regridded
 330 to the M2GMI grid (0.625°×0.5° degrees) using a mass-conserved linear barycentric interpolation
 331 method. The AMF recalculation was performed via:

$$VCD_{new}^{\square} = \frac{VCD_{old}^{\square} AMF_{old}^{\square}}{AMF_{new}^{\square}} \quad (6)$$

332 where VCD_{old} and AMF_{old} are the default states of tropospheric vertical columns and air mass
 333 factors. AMF_{new} is determined by summing the product of scattering weights and the M2GMI partial
 334 columns from the surface to the tropopause level prescribed in the OMI level 2 data.

335 2.3.2. OMI SAO total HCHO columns

336 For the same reason as OMI NO₂, we use OMI SAO total columns based on a newly-
 337 developed algorithm framework by Nowlan et al. (2023). The new retrieval represents a major step
 338 forward in the surface albedo treatment including the bidirectional reflectance distribution function
 339 for land (BRDF) from the MODIS product (MCD43C1 Version 6.1) extended to the UV
 340 wavelengths using a principal component algorithm. Since there are no MODIS BRDF data
 341 available over water, the algorithm uses the Cox-Munk slope distribution to estimate the surface
 342 reflectance of water bodies (Cox and Munk, 1954). An important issue with the long-term record
 343 of OMI HCHO measurements is the artificial increasing trend brought on by sensor degradation
 344 (Choi and Souri, 2015a,b, Gonzalez Abad et al., 2015). The algorithm uses an earthshine spectrum
 345 over the Pacific Ocean with a latitudinal and solar zenith-dependent correction factor described in
 346 Nowlan et al. (2023) to mitigate this artifact.

347 The new SAO algorithm has been validated with Ozone Mapping and Profiler Suite
 348 (OMPS) data radiance with respect to Fourier-transform Infrared Spectroscopy (FTIR) in-situ
 349 measurements in 2012-2020, showing a relative bias of 30% based on monthly-averaged data
 350 (Kwon et al., 2023). While the validation results based on the OMI radiance have not been released
 351 yet, it is likely for the biases to stay at roughly the same range of errors at monthly-gridded OMI
 352 data onto the M2GMI grid which is comparable to the OMPS footprint (50 km).

353 Once again, we used Eq.6 to recalculate OMI HCHO total columns with dynamical shape
 354 profiles produced during the M2GMI simulation. We remove unwanted pixels using the following
 355 criteria: the main quality flag, cloud fraction >40%, and flag for pixels affected by the row anomaly.
 356 We then regridded the data to the MERRA-2 GMI grid using the same approach used for OMI
 357 NO₂.

358 2.4. Experiments

359 We perform a series of experiments to investigate the sensitivity of OH to geophysical
360 variables known to influence or to be tied with OH. Table 2 lists all sensitivity experiments along
361 with their purposes and differences from an analysis (i.e., constrained) experiment. The pillar of all
362 experiments is the analysis experiment (*Sanalysis*) which uses i) chemical variables from a full-
363 chemistry simulation as input to the parameterization of OH in ECCOH (Section 2.1.2; Table 1);
364 ii) transport and metrological fields constrained by MERRA2 reanalysis data (Section 2.1.1); iii)
365 long-term estimates of monthly CO and CH₄ emissions (Section 2.1.2.1 and 2.1.2.2); iv) optical
366 depths of clouds and aerosols along with observed climatology of OMI UV surface albedo; and v)
367 the NO₂ and HCHO fields constrained by the Bayesian data fusion method (Section 2.2.1).

368 To examine the importance of having NO₂ and HCHO fields constrained with OMI data,
369 we design three experiments imitating *Sanalysis*, but withholding the OI scaling factors one at a
370 time. We then subtract these model outputs from those of *Sanalysis* and name them as *SOMInitro*,
371 *SOMIform*, and *SOMInitroform*.

372 The other experiments are intended to systematically isolate the chemical effect of a
373 specific driver/proxy of OH trends. Due to the significant impact of NO₂, tropospheric ozone,
374 stratospheric ozone column, and water vapor on the primary or secondary pathways of OH
375 loss/production (Naik et al., 2013; Murray et al., 2013; Strode et al., 2015; Nicely et al., 2018; Zhao
376 et al., 2020; Anderson et al., 2021), we include four experiments (*SOHwv*, *SOHnitro*,
377 *SOHtropozone*, and *SOHstratozone*) to single out each effect on OH trends. Additionally, we
378 include HCHO (*SOHform*), a robust proxy for VOC oxidation via OH in remote ocean regions
379 (Wolfe et al., 2019) to understand how those chemical pathways have changed over time. In these
380 experiments, we set the target driver constant to the monthly values in the first year of simulation,
381 and subsequently subtract these model outputs from *Sanalysis*. Amongst various OH
382 drivers/proxies studied here, water vapor is simulated online based on the GEOS simulation; to
383 conduct *SOHwv* which aims at isolating the water vapor effect on OH without affecting
384 meteorology, we set water vapor fields fed to the parametrization of OH to the offline MERRA2
385 based on the monthly-varying 2005 simulations. Simultaneously, GEOS is allowed to simulate
386 water vapor online to address meteorology. This ensures that the meteorology remains consistent
387 across both *SOHwv* and *Sanalysis*.

388 Using ambient gas concentrations in the ECCOH model poses a challenge in distinguishing
389 the respective factors contributing to their variations. For instance, it is difficult to discern the
390 distinct influences of lightning-produced NO₂ versus anthropogenic NO₂ on the abundance of OH.
391 However, an advantageous feature of our approach is that various observational sources constrain
392 the data fields used via the Bayesian data fusion method or MERRA2 reanalysis data.

393 **Table 2.** The experiments designed to assess the effect of various OH drivers/proxies and OMI constraints on TOH trends and magnitudes.
 394

Model Scenario	Term	Difference from the analysis run	Purpose
Analysis (<i>constrained</i>)	<i>Sanalysis</i>	--	The “best effort” to simulate the evolution of the CH ₄ -CO-OH cycle from 2005-2019.
Analysis - ^a defaulting to NO ₂ M2GMI	<i>SOMInitro</i>	Uses archived M2GMI monthly-averaged NO ₂ concentration fields.	Isolate the importance of constraining M2GMI NO ₂ concentration fields with OMI observations.
Analysis - defaulting to HCHO M2GMI	<i>SOMiform</i>	Uses archived M2GMI monthly-averaged HCHO concentration fields.	Isolate the importance of constraining M2GMI HCHO concentration fields with OMI observations.
Analysis - defaulting to NO ₂ and HCHO M2GMI	<i>SOMInitroform</i>	Uses archived M2GMI monthly-averaged NO ₂ and HCHO concentration fields.	Isolate the importance of constraining M2GMI NO ₂ and HCHO concentration fields with OMI observations.
Analysis - fixed H ₂ O vapor	<i>SOH_{wv}</i>	The dynamical water vapor fields fed to the parameterization of OH are fixed to the monthly-varying 2005.	Isolate the impact of the long-term trend of water vapor on OH.
Analysis - fixed tropospheric ozone	<i>SOHtropozone</i>	M2GMI ozone fields are set to the monthly-varying 2005.	Isolate the impact of the long-term trend of tropospheric ozone burden on OH.
Analysis - fixed NO ₂	<i>SOHnitro</i>	M2GMI NO ₂ fields are set to the monthly-varying 2005.	Isolate the impact of the long-term trend of NO ₂ on OH.
Analysis - fixed HCHO	<i>SOHform</i>	M2GMI HCHO fields are set to the monthly-varying 2005.	Understand the long-term trend of HCHO strongly tied with VOC oxidation via OH in remote regions.
Analysis - fixed stratospheric ozone column	<i>SOHstratozone</i>	M2GMI stratospheric ozone field fed to the parameterization of OH is set to the monthly-varying 2005.	Isolate the impact of the long-term trend of stratospheric ozone columns on OH.

395 ^a “-“ denotes the subtraction operator.

396 3. Results and Discussion

397 3.1. Spatial distributions and trends analysis of several inputs to the parameterization of OH

398 We begin our analysis with an examination of the long-term trends and magnitudes of two key inputs
399 (HCHO and NO₂) to the parameterization of OH. Some other key parameters, such as total ozone columns,
400 tropospheric ozone columns, and water vapor are also shown in Figure S1-3, Figure S7-8, and Text S1.

401 3.1.1. Tropospheric NO₂ columns

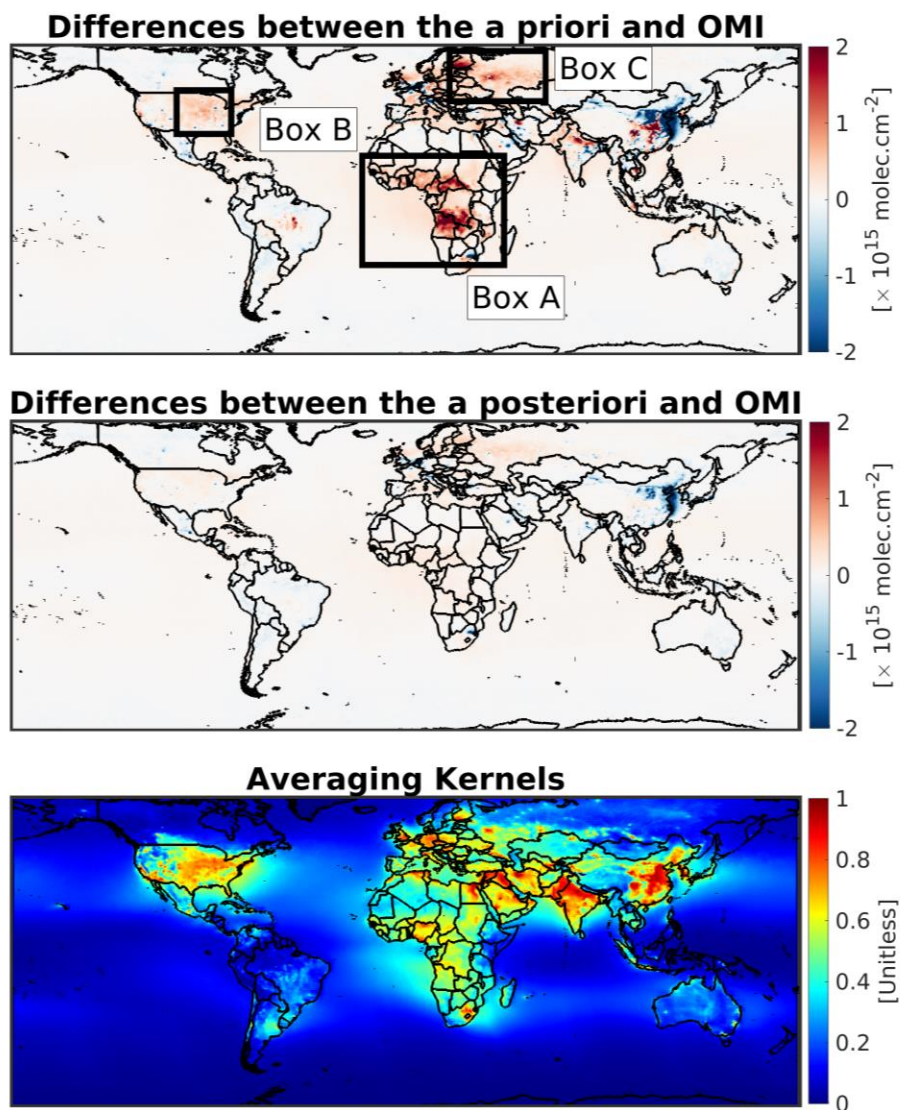
402 We performed two sets of comparisons; the first comparison involves examining the differences in the
403 tropospheric NO₂ columns in the M2GMI relative to those of OMI before and after applying the OI correction.
404 The second comparison focuses on the global 2-D maps of long-term linear trends of OMI, M2GMI prior to
405 and after the Bayesian data fusion correction synched at the satellite viewing condition.

406 Figure 1 demonstrates the absolute difference in M2GMI tropospheric NO₂ columns with respect to
407 those of OMI before (the a priori) and after (the a posteriori) the data fusion application along with AK in
408 2005-2019. In-land regions show positive biases over several regions, including central Africa (box A), the
409 Midwest U.S. (box B), and Europe (box C). The same tendency was observed in Anderson et al. (2021). The
410 largest contributor to NO₂ in box A and box C is biomass burning activities (Jaeglé et al., 2005; Giglio et al.,
411 2012), suggesting that either the emission factors and/or the total dry mass burnt were possibly too high in
412 these regions.

413 M2GMI overestimates NO₂ concentrations in non-urban areas in box B which tend to be more severe
414 during summertime. Although soil NO_x emissions could be the first explanation for this phenomenon,
415 accounting for about 30% of tropospheric NO₂ columns in the region according to Vinken et al. (2014), the
416 soil NO_x parameterization used in M2GMI relies on Yienger and Levy (1995), which is known to have a low
417 bias (Jaeglé et al., 2005; Hudman et al., 2012; Vinken et al., 2014; Souri et al., 2016). Therefore, there may be
418 other uncertainties in the model concerning chemistry (e.g., Canty et al., 2015) or area anthropogenic NO_x
419 emissions (Hassler et al., 2016) causing the bias.

420 A large portion of metropolitan areas in the Middle East, Europe, and the U.S. shows an
421 underestimation of NO₂ in M2GMI. Moreover, OMI observations reveal large positive biases over the North
422 China Plain (NCP), a region exhibiting exceptionally high NO₂ levels (e.g., Duncan et al., 2016; Krotkov et
423 al., 2016; Souri et al., 2017). This is primarily because of not accounting for the recent aggressive emissions
424 mitigation in China in the bottom-up emission inventory used in the model. We observe several regions over
425 China and Yellow Sea underestimating NO₂ with respect to OMI observations that do not improve
426 considerably after the adjustments. This tendency is a result of the use of a fractional error for populating the
427 error covariance matrix of the a priori, rendering the prior error too low. Although we used a regularization
428 factor to battle this problem, it did not vary from region to region. A regionally-adaptive regularization factor
429 could be a possible remedy for this problem but at a cost of overcomplicating the interpretation of the results.

430 Expectedly, the Bayesian fusion greatly mitigates the regional biases, with notable reductions
431 observed over central Africa, China, the U.S., Amazon, and Europe. The regional biases (>80%) well exceed
432 the reported biases associated with OMI tropospheric NO₂ product (<40%), suggesting that the adjustments
433 should be considered as improvement. Nonetheless, it is important to acquire an abundance of long-term
434 records from surface spectrometers such as MAX-DOAS and Pandora to comprehensively evaluate the degree
435 of enhancement of M2GMI constrained by OMI within the troposphere, which is currently unavailable for the
436 period of 2005-2019 to our best knowledge. The reduction in the biases over remote areas in the tropics is less
437 noteworthy due to large errors in the observations. In other words, it is difficult to have high confidence in the
438 degree of deficiency the model can have in simulating NO₂ over pristine areas by comparing it to OMI. This
439 notion mathematically manifests in low AK in remote areas showing that rich information from OMI
440 tropospheric NO₂ gravitates more towards polluted regions. This finding assumes that the regularized
441 covariance matrix of the prior error does not substantially vary between land and ocean and is isotropic.

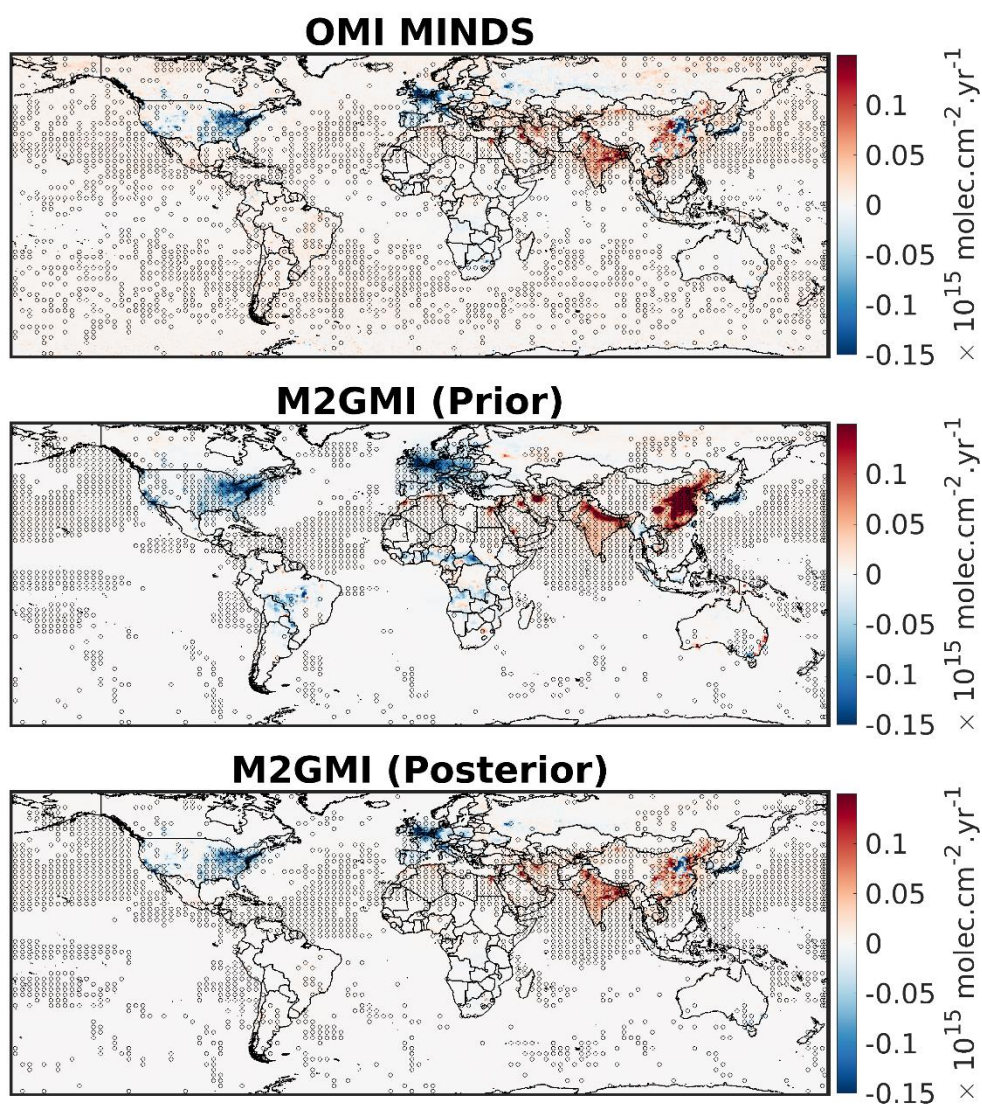


442
 443 **Figure 1.** The global maps of M2GMI tropospheric NO₂ annual difference with respect to those of OMI before
 444 applying the Bayesian data fusion correction factors (top) and after (middle) in 2005-2019; the mean of
 445 averaging kernels describing the gained information from OMI (bottom). Grids in high latitudes are removed
 446 from the figure due to too few numbers of samples OMI provided.
 447

448 Figure 2 illustrates the linear trends of tropospheric NO₂ between 2005 and 2019 observed by OMI
 449 and simulated by the M2GMI before and after using the OI algorithm. The errors in OMI observations and the
 450 constrained M2GMI are considered while calculating the trends. Focusing on the trends by OMI, we observe
 451 a consistent picture compared to former studies (Duncan et al., 2016; Choi and Souri, 2015a,b; Krotkov et al.,
 452 2016; Jin and Holloway, 2015; Souri et al., 2017). High income countries, such as the U.S., those located in
 453 the western Europe, and major cities in Russia, undergo a significant reduction of NO₂ concentrations due to
 454 the implementation of emission mitigation regulations. Additionally, low and moderate income countries, such
 455 as those in the Middle East, northern Africa, and India, have seen upward trends in NO₂. Various signs of
 456 trends are observed in East Asia. Due to recent effective regulations in China (Zhang et al., 2012), we observe
 457 downward trends in the NCP region (Rueter et al., 2014; de Foy et al., 2016; Souri et al., 2017). The downward
 458 trend predominantly starting from 2011-2012 counteracts the upward trend in prior years resulting in

459 statistically insignificant linear trends. Both Japan and South Korea show downward trends during the period
460 of 2005-2019 (Duncan et al., 2016; Souri et al., 2017).

461 Encouragingly, the model prior simulation of the tropospheric NO₂ trend is consistent with OMI over
462 most of the polluted regions except for China, where the bottom-emission inventories used in the M2GMI fail
463 to reflect recent mitigation efforts occurring in NCP region. The posterior estimation is in a higher degree of
464 agreement compared to OMI (Text S2). An encouraging observation arising from the comparison of the
465 M2GMI prior with the posterior NO₂ trends is the achievement of a higher spatial variance (information) in
466 low and medium income countries (e.g., India and Iran). This finding suggests that the emission inventories
467 used in the M2GMI lacked adequate spatial information even at the model spatial resolution.

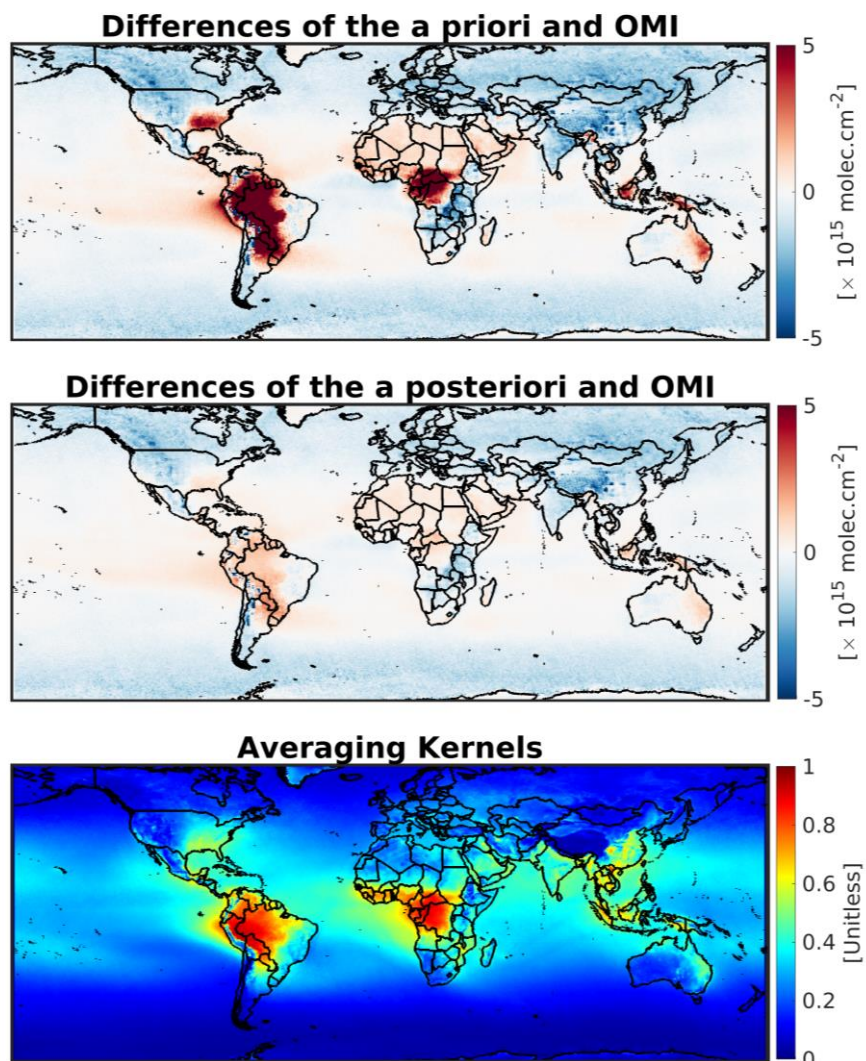


468 **Figure 2.** The global maps of linear trends of annual tropospheric NO₂ columns observed by OMI and
469 simulated by M2GMI before and after using the Bayesian fusion. The model simulations are sampled at the
470 exact time and location of OMI, and masked if OMI observations were unavailable due to data quality
471 criteria used. The dots indicate statistically significant trends at 95% confidence interval.
472
473

474 3.1.2. Total HCHO columns

475 We validate the simulated HCHO concentrations, drawing inspiration from the NO₂ comparison
476 framework. Figure 3 illustrates the absolute differences in simulated HCHO total columns with respect to OMI
477 before and after the Bayesian data fusion application, in addition to AK. The prior model simulation has
478 considerable skill in capturing the HCHO total columns over several areas, such as the Middle East, Europe,
479 India, and East Asia. However, marked positive biases are discernible in regions with abundant isoprene
480 emissions, such as the Amazon, southeast Asia, southeast U.S., and central Africa. This outcome is most likely
481 due to an overestimation of biogenic emissions; various investigations have reported a predominantly positive
482 bias (between a factor of 2 to 3) linked to isoprene emissions estimated by the Model of Emissions of Gases
483 and Aerosols from Nature (MEGAN) using satellite measurements in isoprene-rich regions (e.g., Millet et al.,
484 2008; Stavrou et al., 2009; Marais et al., 2012; Bauwens et al., 2016; Souri et al., 2020a).

485 The simulated HCHO concentrations are relatively too low over pristine areas, such as high latitudes
486 and over mountains. This may be attributed to an underestimation of CH₄ in M2GMI because of assigning its
487 values as background conditions (Strode et al. 2019). The integration of OMI satellite data has proven effective
488 at reducing the biases in areas where HCHO concentrations are large because the signal-to-noise ratio tends to
489 be large resulting in high AKs. Nonetheless, there are some adjustments over remote areas. In fact, OMI HCHO
490 columns provide more information than OMI NO₂ in remote areas because background HCHO concentrations
491 are not extremely low due to evenly distributed methane and methanol concentrations. It is worth noting that
492 the biases in M2GMI well exceed the expected OMI HCHO column biases, suggesting that the adjustments to
493 HCHO improve the model.



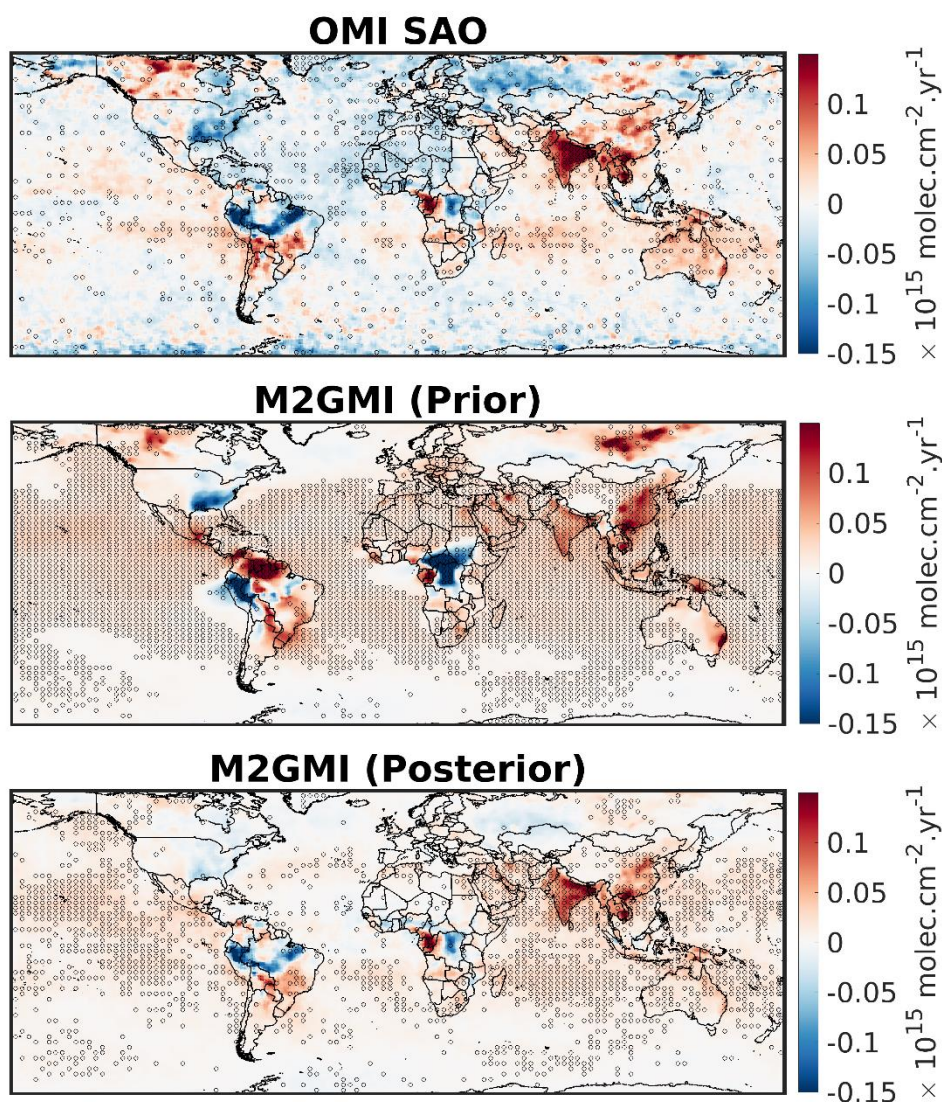
494
495 **Figure 3.** Same as Figure 1 but for HCHO total columns.

496 Figure 4 shows the global maps of HCHO total column trends derived from OMI, the prior M2GMI,
497 and the posterior M2GMI. The widespread upward trends in HCHO over India are evident due to lack of
498 effective efforts on cutting emissions related to volatile organic compounds (e.g., De Smedt et al., 2015;
499 Kuttippurath et al., 2022; Bauwens et al., 2022). We observe HCHO columns going up in the northwestern US
500 and over oil sands in Canada, possibly due to increased evergreen needleleaf forest and an increase in crude
501 oil production (Zhu et al., 2017), respectively. The downward trends over the southeast US could be due to a
502 decrease in drought events (Figure S5), which significantly affect isoprene emissions and the oxidation of
503 VOCs (Duncan et al. 2009; Naimark et al., 2021; Wang et al., 2022). Alternatively, this downward trend could
504 be partially due to the dampened HCHO production from VOC oxidation due to reduced NO_x emissions
505 (Marais et al., 2014; Wolfe et al., 2016; Souri et al., 2020c). In agreement with previous studies (Stavrakou et
506 al. 2017, Souri et al., 2017, Shen et al., 2019, Souri et al., 2020a), HCHO columns increase over the NCP.
507 HCHO columns tend to decrease over parts of central Africa (e.g., Democratic Republic of the Congo) and the
508 Amazon basin potentially due to reduced deforestation rates (De Smedt et al., 2015; Jones et al., 2022).
509 However, a large variability in the sign of HCHO trends over these regions is seen; Congo shows an opposite
510 trend in comparison to that of Democratic Republic of the Congo; the northern portion of the Amazon basin
511 increased. Encouragingly, the prior knowledge captures the upward trends over India and China along with

512 downward trends over central Africa. However, the magnitudes and spatial features of these trends are not
513 entirely in line with respect to OMI.

514 We do not fully understand HCHO trends over oceans. Part of these patterns might be caused by
515 transport from nearby sources. For instance, areas around south Asia, South America, and Gulf of Mexico can
516 be affected by the trends over the land in their proximity. However, trends over several areas, such as the
517 southern part of the Indian Ocean, Australia, and Sahara, are not fully explainable by nearby sources. It is
518 possible that certain patterns can be linked to climate variability or OH (Wolfe et al., 2019) affecting the
519 oxidation of background VOCs; an in-depth understanding of HCHO trends over oceans certainly deserves a
520 separate follow-up study.

521 The posterior estimates better line up with the OMI trends, especially over the Amazon, India, and
522 Central Africa (Text S3). The correction factors, however, worsen the trends over the southeast US and
523 Canada. One possible explanation for this may be the varying errors from the data fusion algorithm, which
524 tend to be reduced more in summertime than in wintertime due to the larger OMI HCHO signal. This results
525 in some degree of inconsistencies of the linear trend over these regions with larger interannual and interdecadal
526 variabilities.



527

528 **Figure 4.** Same as Figure 2 but for total HCHO columns. The linear trends in OMI SAO are smoothed by a
529 median filter for better visualization.

530

531 In sum, we saw that M2GMI NO₂ and HCHO, both inputs to the parameterization of OH, were broadly
532 better presented through the integration of OMI observations. Consequently, the improvement is expected to
533 elevate the level of reliability in the experimental outcomes, particular in the context of *SOHnitro* and
534 *SOHform* simulations. As for other important compounds, such as stratospheric columns, tropospheric O₃, and
535 water vapor, the comparison of the model with OMI total ozone columns shows a strong degree of agreement
536 (<4% biases) with no significant trend in low-mid latitudes (Figure S1 and S2). The well-documented upward
537 trend in tropospheric ozone in the northern hemisphere is well reproduced by M2GMI (Figure S3). We did not
538 validate GEOS water vapor simulations, because of the use of MERRA2 reanalysis, which is thoroughly
539 validated in Bosilovich et al. (2017). Furthermore, the comparison of integrated water vapor linear trends from
540 our GEOS-5 run (2005-2019) with satellite data presented in Borger et al. (2022) shows a remarkable
541 agreement (Figure S7-8).

542 3.2. Added value of OMI on simulated tropospheric OH

543 Here, we present the results from three OMI-related experiments (*SOMInitro*, *SOMIform*,
544 *SOMInitroform*) to understand the effect of OMI adjustments made to M2GMI on TOH. Moreover, we
545 calculate the response of TOH to NO₂ and HCHO using Eq.5.

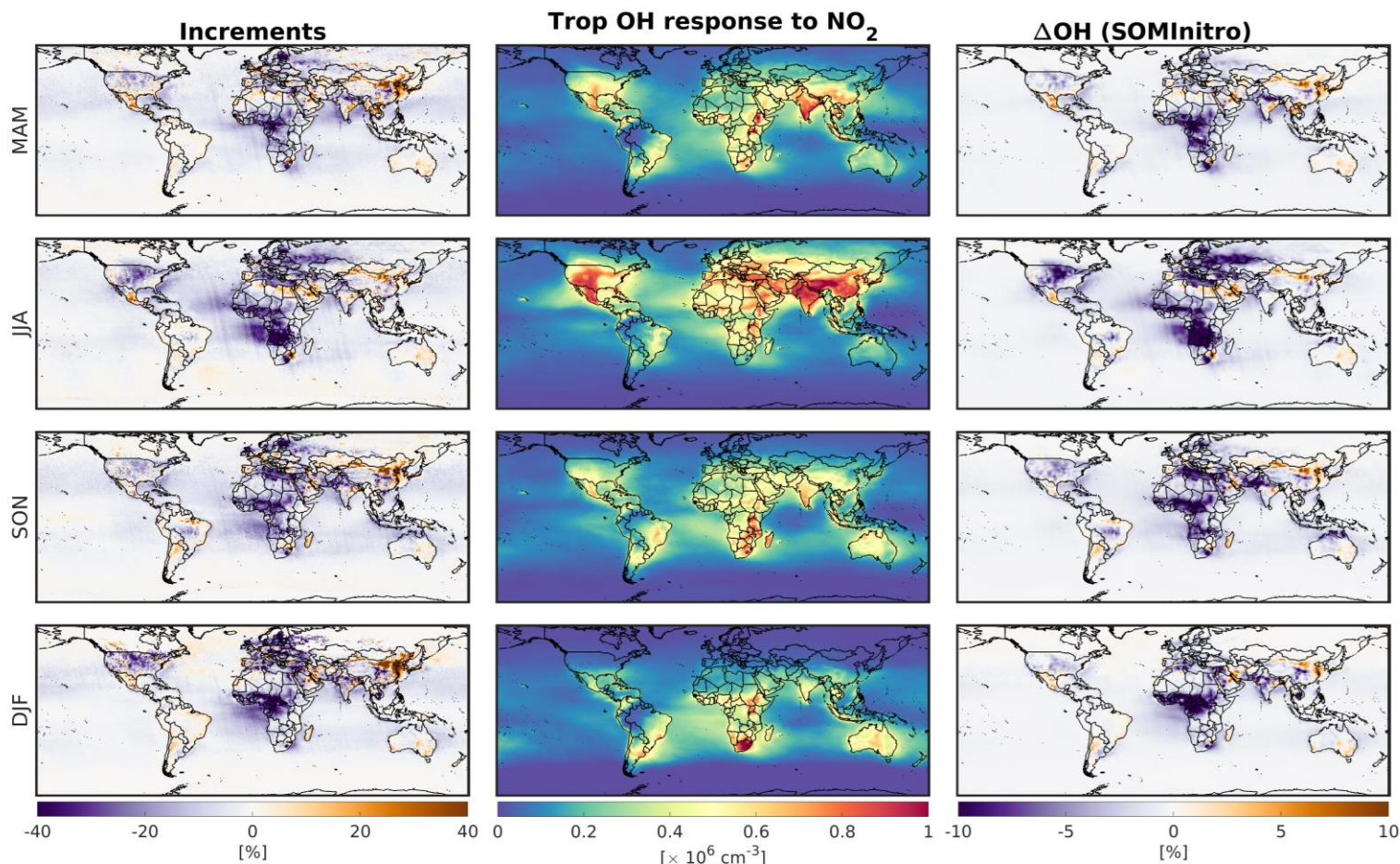
546 Figure 5 consists of three columns, illustrating the percentage adjustments made by OMI NO₂ using
547 OI, the response of TOH to NO₂ concentrations, and the simulated TOH derived from the *SOMInitro*
548 experiment. The observed pattern of increments aligns with the improvements seen in Figure 1, with positive
549 (negative) values indicating underestimation (overestimation) of M2GMI. Broadly, the overestimates
550 dominate over underestimates resulting in the global tropospheric NO₂ reduction by ~4%. Upon segregating
551 the increments into four distinct seasons, it becomes evident that the adjustments do not uniformly apply to
552 every season. This non-uniformity is primarily attributed to biases in M2GMI, influenced by biomass burning
553 (box A, C) (Section 3.1.1), both of which exhibit strong seasonality.

554 Deciphering the precise chemical processes influencing the response of OH to NO₂ using a machine-
555 learning approach is challenging. However, it is widely recognized that reactive nitrogen has positive feedback
556 on tropospheric OH through increased NO+HO₂ and ozone (Murray et al., 2021; Zhao et al., 2020; He et al.,
557 2021). Considering NO₂ as a surrogate for reactive nitrogen, similar tendencies are expected, as evident from
558 the positive numbers from the sensitivity results obtained from offline calculations. The response of TOH to
559 NO₂ displays a pronounced seasonal cycle stemming mainly from photochemistry. It is believed to have some
560 negative values for the sensitivity of OH to NO₂ for extremely polluted regions due to radical termination
561 through NO₂+OH or ozone titration (Nicely et al., 2018). While we have not identified any negative values in
562 the tropospheric domain, we have observed significant negative values of OH when perturbing NO₂ at the
563 model surface layer (Figure S26). This tendency highlights the ECCOH's ability to account for non-linearities.

564 The impact of adjustments made by OMI NO₂ on TOH is most substantial over regions where both
565 the adjustments and TOH responses to NO₂ are significant. For instance, the large adjustments made over
566 Europe in DJF do not substantially affect TOH because the response value is low due to reduced
567 photochemistry.

568 On a global scale, changes to TOH are much milder (1% reduction) than those occurring regionally.
569 For instance, we see substantial regional impacts (up to 20%) over many areas such as Central Africa, the
570 Midwest US, the Middle East, and Eastern Europe. In light of the global reduction in OH, we observe global
571 column average methane mixing ratios (XCH₄) to increase by 10 ppbv on average (Text S4). This
572 augmentation happens monotonically with an increase of 0.9 ppbv per year, ultimately resulting in ~15 ppbv
573 difference at the end of the simulation (Figure S13). This is essentially due to the long lifetime of CH₄.
574 Likewise, the TOH reduction results in column average CO mixing ratio (XCO) enhancements which transpire

575 more locally than XCH₄ does due to the shorter XCO lifetime. The XCO enhancements reach above 10 ppbv
 576 in Africa (Text S5).
 577
 578



580 **Figure 5.** (first column) the percentage of adjustments applied to M2GMI NO₂ fields within the troposphere
 581 suggested by OMI tropospheric NO₂ columns for four different seasons, (second column) the semi-normalized
 582 response of tropospheric OH to tropospheric NO₂ changes based on ECCOH offline calculations, and (third
 583 column) the resulting effect of the adjustments on tropospheric OH derived from the online simulation
 584 (*SOMInitro*). MAM, JJA, SON, and DJF are acronyms for March-April-May, June-July-August, September-
 585 October-November, and December-January-February.
 586

587 Figure 6 demonstrates the same scheme as Figure 5 but with a focus on the *SOMIform*. Marked
 588 negative increments are found in regions characterized by elevated isoprene concentrations because of the
 589 overestimations of M2GMI biogenic isoprene emissions. Positive increments are mostly confined to high
 590 latitudes and certain areas of East Asia (Section 3.1.2).

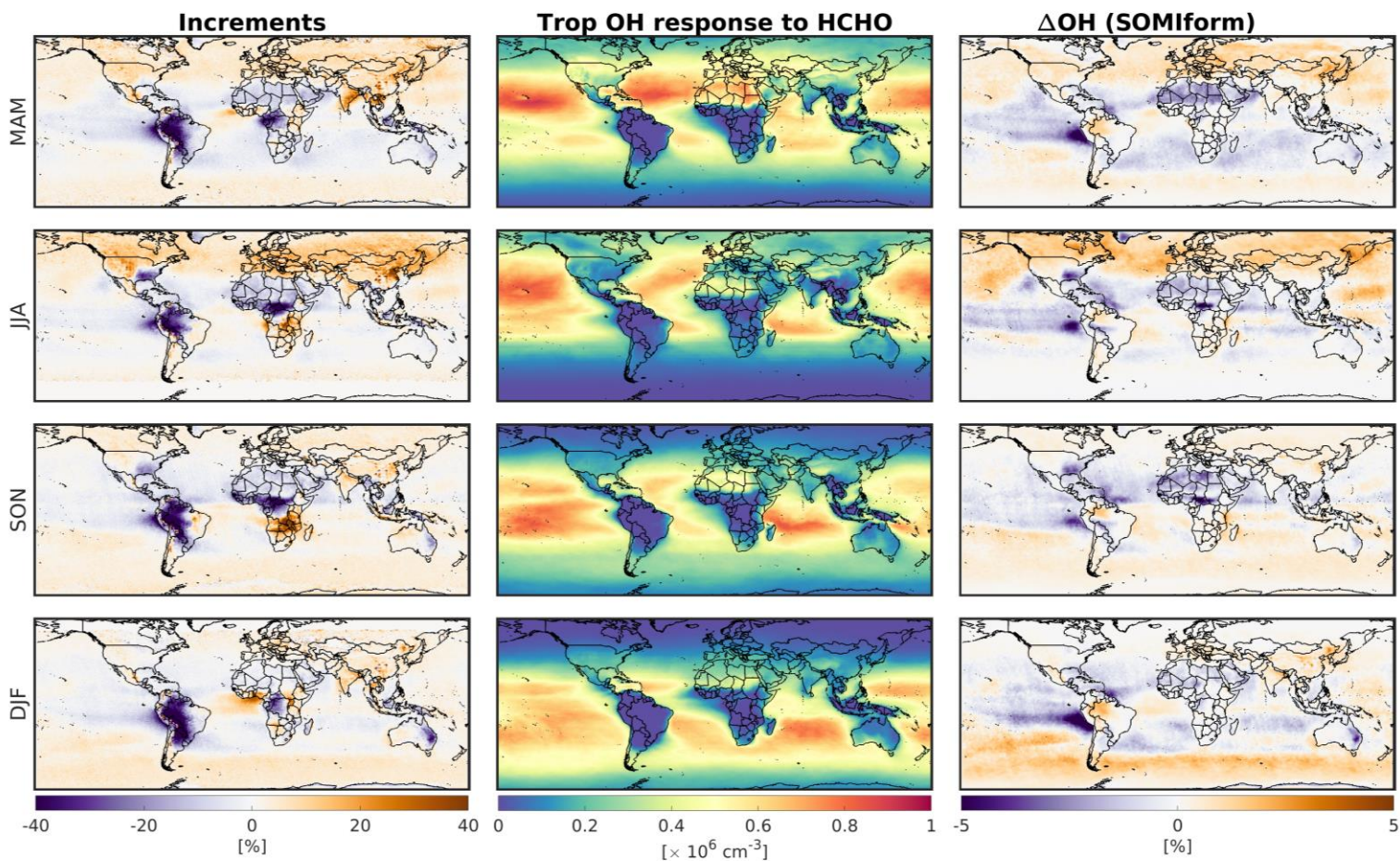
591 The interplay between HCHO and OH is contingent on the intricate dynamics governing HCHO
 592 production from the oxidation of VOCs and methane and HCHO loss from various chemical pathways (Valin
 593 et al., 2016; Wolfe et al., 2019). In remote areas where HO_x is low, the prevailing sink of HCHO is through
 594 photolysis. Conversely, in more polluted areas, the reaction of HCHO+OH emerges as a competing loss
 595 pathway. Assuming a steady-state approximation, which is a reasonable assumption for pristine areas, the
 596 photolysis loss of HCHO dominates over the reaction with OH, resulting in a linear relationship between
 597 HCHO and OH. In other words, high (low) HCHO concentrations are indicative of high (low) TOH. It is

598 because of this that we use HCHO as a proxy of TOH in remote oceans regions. In regions characterized by
 599 heightened HO_x levels, OH and HCHO become decoupled. Encouragingly, our implicit parametrization of OH
 600 has considerable skill at elucidating these intricate chemical tendencies; specifically, it reveals muted
 601 responses in regions with relatively tangible pollution levels, whereas positive responses are evident in oceanic
 602 regions. Like results obtained for NO_2 , the response map has a seasonal cycle due to photochemistry.

603 Because of the muted response of TOH to HCHO over land, a substantial portion of geographical
 604 regions undergoing significant adjustments made by OMI becomes less important. TOH primarily changes
 605 over oceanic areas in a way that it decreases in low latitudes but increases in high latitudes. The largest
 606 reduction occurs in Amazon downwind where both increments and responses display large magnitudes. As a
 607 result of these changes, we see a marginal increase in XCH_4 over tropics where OMI increments reduced TOH.
 608 The HCHO adjustment did not noticeably affect XCO either (Text S5).

609 Modifications on HCHO by OMI do not signal substantial changes in background VOC oxidation
 610 through OH. In fact, TOH changes by this proxy are of an order of magnitude less than those by OMI NO_2 .
 611 This tendency is a result of two key factors: i) the adjustments wield their major influence over oceans where
 612 M2GMI has a fair performance, and ii) the amount of information obtained from OMI HCHO (i.e., AK)
 613 remains somewhat limited in remote areas due to low signal-to-noise ratios.

614 Due to the rather independent nature of the TOH responses to NO_2 and HCHO, where the former
 615 prevails over land and the latter over ocean, the concurrent adjustments of HCHO and NO_2 using OMI (i.e.,
 616 *SOMInitroform*) results in a rather linear combination of outcomes derived from *SOMIform* and *SOMInitro*
 617 (Figure S21). This linear outcome is characterized by a large decrease in TOH in low latitudes and a moderate
 618 increase in high latitudes resulting in a decrease of global TOH by $\sim 1\%$.



620 **Figure 6.** Same as Figure 5 but for HCHO.

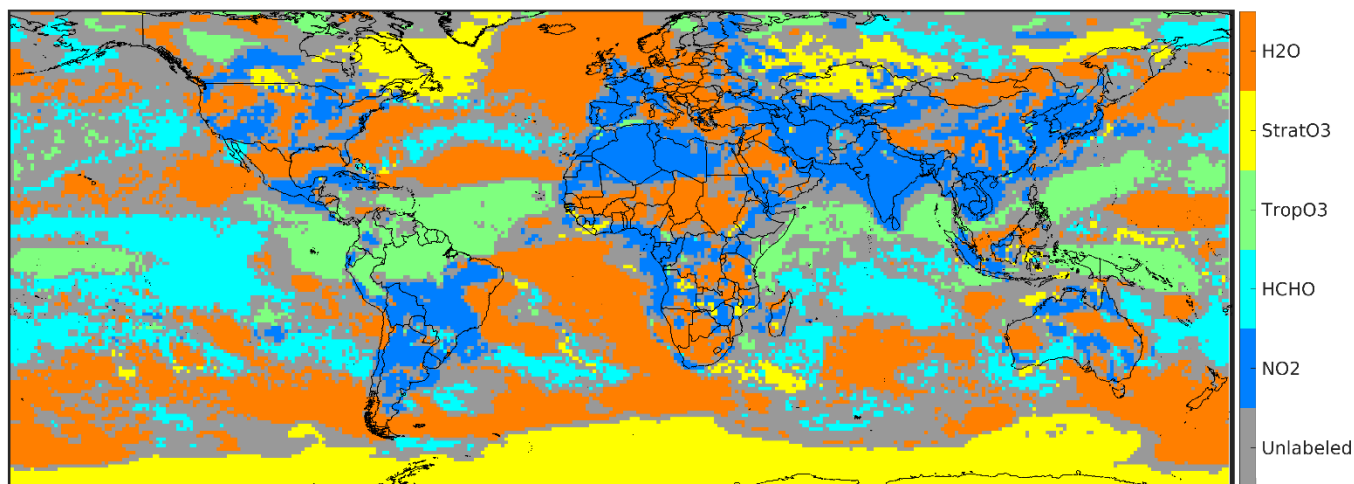
621 3.3. Synergy of the model and satellite observations to explain TOH long-term trends

622 3.3.1. The dominant contributor to TOH trends

623 Here, we take advantage of the wealth of information from satellites and our well-characterized model
624 used for the inputs to the parameterization of OH to rank the dominant contributor to TOH linear trends. By
625 assuming that TOH follows a linear combination of each individual experiment designed to isolate OH
626 driver/proxy (i.e., *SOHnitro*, *SOHform*, *SOHtropozone*, *SOHstratozone*, and *SOHwv*), wherein second (or
627 higher) chemical feedback is disregarded, we can determine the biggest contributor to the TOH trend for each
628 model grid box by finding which driver/proxy holds the largest absolute amount. We only label a grid if the
629 absolute linear trend of the dominant driver/proxy surpasses the second most dominant one by 30%.

630 Figure 7 illustrates the dominant factor explaining TOH trends. Several patterns can be found from
631 this result: i) NO₂ plays a significant role in TOH trends in various polluted areas, such as Asia and the Middle
632 East; ii) the upward trend of TOH over the western Pacific Ocean is primarily attributed to increased
633 tropospheric ozone from Asia (e.g., Lin et al., 2017); also, we observe a significant fraction of TOH over the
634 tropical Atlantic Ocean increasing because of rising tropospheric ozone from Africa and Central/South
635 America (Edwards et al., 2003); iii) HCHO is convolved with TOH trends over tropical oceans; iv) water
636 vapor plays a pivotal role in shaping TOH trends over oceans across the globe; iv) stratospheric ozone columns
637 are mostly significant over the South Pole due to the ozone healing process (Figure S2). The next sections will
638 focus on the magnitude of these trends and the degree to which they can collectively explain the variance in
639 TOH trends compared to *Sanalysis*.

640 It is important to recognize that the analysis presented here should be interpreted as a relative
641 assessment of a limited number of TOH drivers/proxies, rather than an exhaustive evaluation of all the physical
642 and chemical processes that are tied to TOH. Nonetheless, the data presented offers valuable insights into the
643 TOH trends and can be used as a basis for further research.
644



645 **Figure 7.** The major contributor to TOH trends based on the largest absolute trends of TOH drivers/proxies
646 above 30% of the second most dominant factor.
647

648 3.3.2. Magnitudes of linear trends of TOH key inputs

649 Figure 8 shows the linear TOH trends influenced by NO₂ (*SOHnitro*), HCHO (*SOHform*), water
650 vapor (*SOHwv*), tropospheric ozone (*SOHtropozone*), and stratospheric ozone (*SOHstratozone*). A
651 discussion on each parameter will follow:

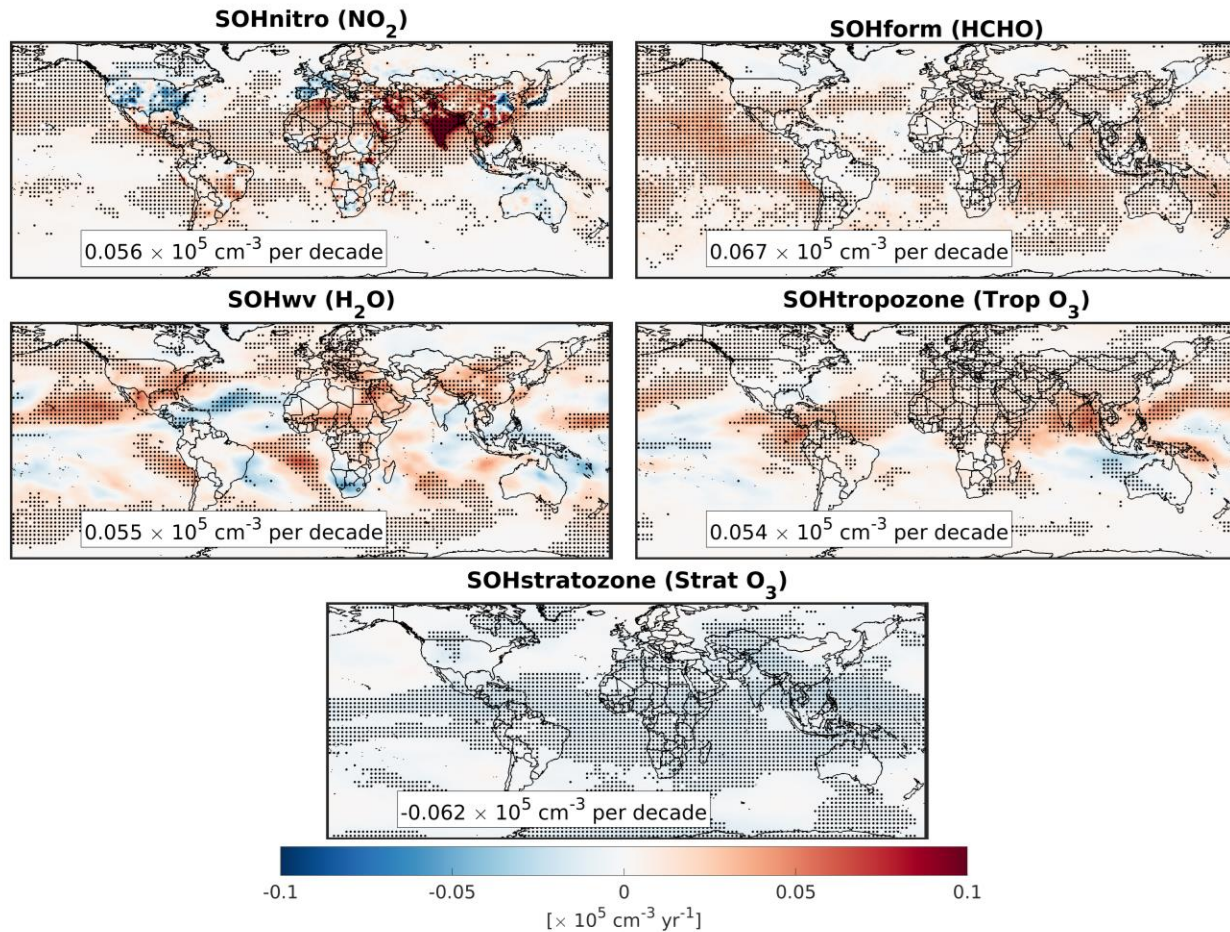
652 *SOHnitro* – The trends in TOH driven by NO₂ show a strong correlation with the a posteriori trend
653 discussed in Section 3.1.1, with low- and medium-income countries experiencing an increase in TOH due to
654 rising NO₂ levels, while high-income countries see a reduction in TOH due to the opposite trend. The most
655 significant increase in TOH is observed over India, where both the NO₂ trend and TOH sensitivity to NO₂ are
656 prominent. The most rapid regional decline in TOH seems to be over the NCP, because of NO_x reductions that
657 began after 2011. This finding is particularly noteworthy since M2GMI did not reproduce this trend without
658 OMI as a constraint. The trend in TOH resulting from NO₂ is predominantly anthropogenic in nature. This
659 aligns with the findings of Chua et al. (2023), who observed that the impact of lightning NO_x emissions on
660 TOH trends was relatively minor. The global trend in TOH driven by NO₂ is positive, but with considerable
661 variation due to the significant disparities in how anthropogenic NO_x emissions have changed.

662 *SOHform* – We saw that HCHO was a reasonable proxy for TOH over oceans. Accordingly, the TOH
663 trends primarily are observed over oceans, especially over the Pacific and the Indian Oceans. This lines up
664 with the information gathered from the analysis of M2GMI and OMI HCHO observations (Figure 4). These
665 upward HCHO trends, as discussed in Section 3.1.2, may be influenced by transport and dynamics. It is worth
666 noting that the increase in TOH tied to this proxy (HCHO) is a global tendency, attributable to the relatively
667 uniform rise in HCHO levels across oceans.

668 *SOH_{wv}* –Water vapor is a primary source of OH. The offline sensitivity of ECCOH captures this
669 tendency (Figure S22). Accordingly, the TOH linear trends mirror those of IWV (Figure S8) with major
670 increases over oceans. Similar to other experiments, the global TOH increases because of rising water vapor
671 in the atmosphere. We acknowledge that understanding the reasons for changes in water vapor, which our
672 model shows to agree with Broger et al. (2022), is a complex subject that goes beyond the scope of our research.
673 It requires an in-depth understanding of the water cycle, evapotranspiration and precipitation rates, and the
674 effect of temperature on the air's capacity to hold moisture, known as the Clausius Clapeyron relationship.
675 However, a great deal of effort has been made to demonstrate that global water vapor levels have increased
676 significantly in recent decades. This is based on reanalysis data, microwave satellites, and in-situ
677 measurements (Trenberth et al., 2005; Chen and Liu, 2016; Wang and Liu, 2020; Allan et al., 2023), which is
678 consistent with what our model shows, as it is well-constrained by MERRA2 reanalysis data.

679 *SOHtropozone* – The impact of tropospheric ozone on OH formation is widely acknowledged
680 (Lelieveld et al., 2016). Likewise, our ECCOH offline sensitivity tests have revealed a largely positive
681 correlation between tropospheric ozone and OH (Figure S23). Consequently, the linear trends observed in
682 TOH closely mirror those of tropospheric ozone in M2GMI (Figure S3). This tendency is especially noticeable
683 in the Atlantic Ocean, East and Southeast Asia, as well as the northern region of the Pacific Ocean, where
684 rising ozone levels have increased TOH. M2GMI suggests that tropospheric ozone levels in the southern
685 hemisphere have decreased (Text S1), potentially leading to a downward trend in TOH, an observation that
686 has yet to be fully confirmed (e.g., Thompson et al., 2021). This finding is especially important given past
687 research indicating that models tend to exaggerate TOH asymmetry between the northern-southern
688 hemispheres (Strode et al., 2015; Naik et al., 2013). The decrease in the simulated tropospheric ozone may
689 offer a plausible explanation for this tendency, but further verification is deemed necessary. Like the previous
690 experiments, tropospheric ozone on average leads to a global increase in TOH in 2005-2019.

691 *SOHstratozone* –Stratospheric ozone columns reduce UV actinic fluxes leading to a reduction in
692 tropospheric JO¹D and thus OH, a tendency well reproduced by ECCOH (Figure S24). Nonetheless,
693 stratospheric columns did not change noticeably in the tropics and mid-latitudes where OH production is
694 important; consequently, the linear trends are close to zero or faintly negative due to a slight upward trend in
695 the column. This tendency results in a rather uniform decrease of TOH globally.

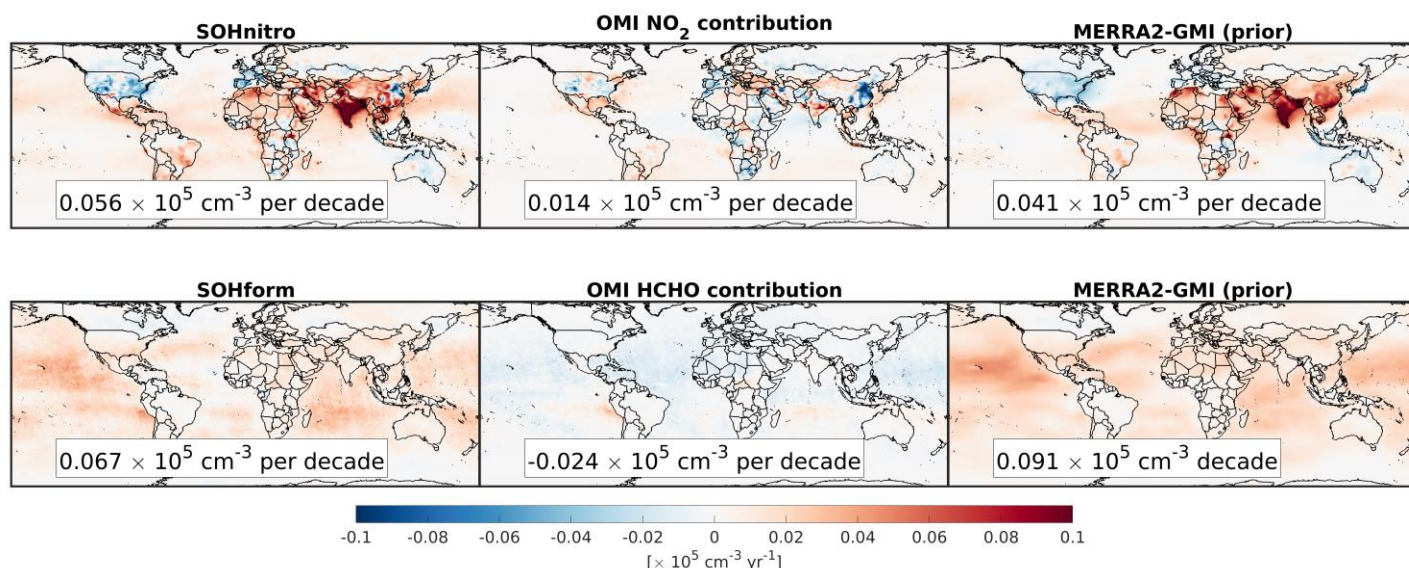


696
697
698
699
700
701
702

Figure 8. The contribution of each TOH key input (addressed in this study) to TOH in 2005-2019. HCHO, NO₂, and water vapor results are observationally constrained. Stratospheric ozone columns yielded comparable results compared to total ozone columns observed by OMI, however a large portion of tropospheric ozone trend has remained unverified in the southern hemisphere. ENSO affects the variability of TOH (Anderson et al., 2021), so we add a linear term to Eq.4 that is a function of the Niño 3.4 Index. This helps prevent ENSO from affecting the subsequent results.

703 3.3.3. OMI contributions to TOH trends

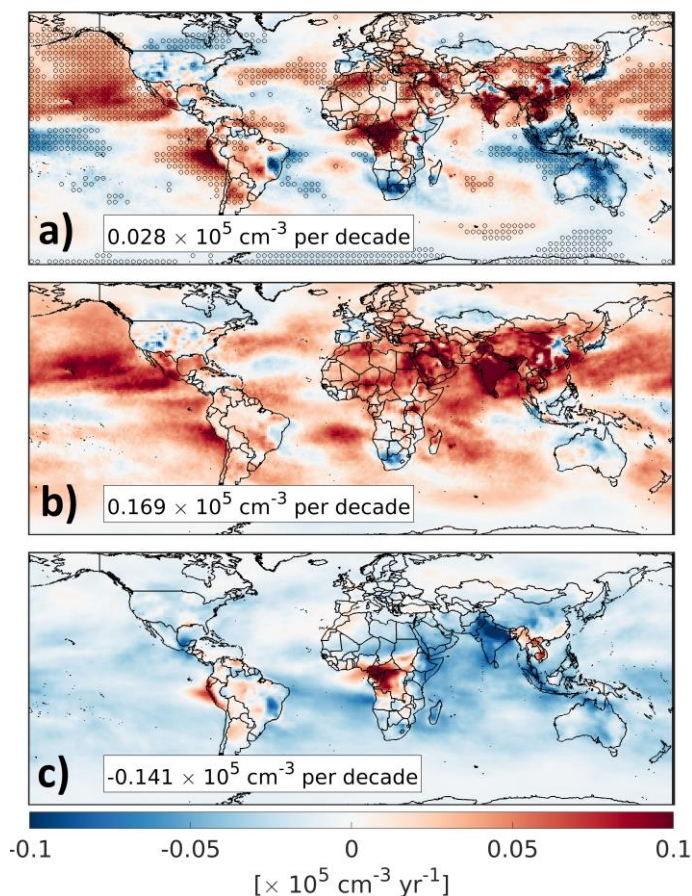
704 It is attractive to gauge the additional information gained from OMI on better representing the linear
705 trends of TOH. To achieve this, we need to analyze three sets of model output: one with OMI scaling factors,
706 one without OMI scaling factors, and one with the NO₂ and HCHO drivers (i.e., *SOHnitro* and *SOHform*). The
707 linear trends from these sets of model results are shown in Figure 9. The trends in the first column illustrate
708 the overall effect of NO₂ and HCHO on TOH trends, while the two other subplots isolate the effect of OMI
709 from the prior information based on M2GMI. M2GMI plays a significant role in shaping the trends in
710 *SOHnitro*, possibly due to the small discrepancy between the trends in OMI and M2GMI columns over regions
711 where TOH is responsive to the driver. The most significant impact of OMI on NO₂ is visible over NCP.
712 Concerning HCHO, OMI slows down the upward trends in TOH over oceans which was suggested by M2GMI.
713 In general, M2GMI largely dictates the overall shape of TOH trends driven by NO₂ and HCHO possibly due
714 to small difference between the model and OMI observations and/or limited informational content in OMI.



715
 716 **Figure 9.** The resulting effect of tropospheric NO₂ and HCHO on TOH linear trends during 2005-2019 (first
 717 column); the contributions of OMI information added on top of the prior knowledge (M2GMI) (middle
 718 column); the effect of the prior knowledge on shaping TOH linear trends (last column).

719 *3.3.4. How well can these experiments explain the simulated trends collectively?*

720 We find that there is a good degree of correlation between the sum of the linear trends and those of
 721 *Sanalysis* ($R^2=0.65$) indicating that a good portion of variability in TOH trend can be well explained by these
 722 experiments (Figure S25). Figure 10a shows the linear trend of TOH from *Sanalysis* in 2005-2019, and Figure
 723 10b shows the sum of the linear trends of the five OH key inputs. These maps are one of the most recent and
 724 detailed TOH trends available, relative to newer studies (Nicely et al., 2018; Zhao et al., 2020; Chua et al.,
 725 2023). The TOH trend from *Sanalysis* varies greatly, where positive values are prevalent over northern parts
 726 of the Pacific Ocean, the Middle East, central Africa, and several regions over East Asia. Negative trends are
 727 found over the US, southeast Asia, and the southern part of the Pacific Ocean. The linear sum of the
 728 experiments strongly aligns with *Sanalysis*, particularly over the northern hemisphere, reinforcing that the
 729 selected parameters are sensible choices to reproduce a large portion of variance in TOH trend.



730
 731 **Figure 10.** (a) The linear trends derived from *Sanalysis* experiment, the “best effort” to simulate the evolution
 732 of the CH₄-CO-OH cycle, from 2005-2019. The statistically significant trends are superimposed by dots. (b)
 733 The linear summation of the five selected TOH influencers including water vapor, NO₂, HCHO, stratospheric
 734 and tropospheric ozone, showing a strong degree of correspondence to the top panel, particularly in the
 735 northern hemisphere. (c) The unexplained portion of the TOH trends, which was not explainable by five
 736 experiments addressed in this research.

737
 738 Revealing the unexplained portion of TOH trends, which cannot be attributed to the selected TOH
 739 experiments, is necessary. Within the model, various physiochemical factors such as CO, CH₄, dynamics,
 740 aerosols, and clouds can impact the TOH trends. Although we will not delve into these drivers in this study,
 741 we can identify unexplained parts of TOH trends by subtracting the sum of trends derived from the five primary
 742 TOH key inputs from those of *Sanalysis*, which discounts second (or higher) chemical feedback. Figure 10c
 743 displays the unexplained TOH trends between 2005 and 2019. It is readily apparent that there are uniform and
 744 significant downward trends in TOH in the tropics and subtropics where photochemistry is strong. This is most
 745 likely triggered by increasing concentrations of CH₄, which is demonstrated in Figure S10, causing OH levels
 746 to decrease over time. It is very probable that the extent of these downward trends in TOH has been exaggerated
 747 in our model because of the simulated CH₄ increasing too rapidly compared to in-situ observations. The
 748 overestimation of the upward trend in CH₄ in our model compared to in-situ observations could be caused by
 749 the biases (~3%) in sources minus sinks and/or the initial condition. Consequently, the globally-averaged TOH
 750 trend derived from *Sanalysis* may be slower than it should be. Lastly, an unexplained strong upward trend in
 751 TOH over central Africa lingers.

752 4. Conclusion

753 While a comprehensive multi-sensor/multi-species data assimilation and inverse modeling approach,
754 such as Souri et al. (2020a), Miyazaki et al. (2020), and Souri et al. (2021), would be ideal for fully harnessing
755 the potential of satellite information on improving multiple aspects of a model representing OH, it will be
756 prohibitively expensive. Therefore, our simplified approach serves the purpose of understanding the first-order
757 effects of observational adjustments to TOH drivers/proxies before committing substantial resources to the
758 implementation/execution of an observationally-constrained, full-chemistry model. Here, we implemented the
759 newest version of the parameterization of OH, following Anderson et al. (2022), within NASA's GEOS model,
760 presenting an opportunity to understand and mitigate TOH biases caused by misrepresentation of HCHO and
761 NO₂ concentrations with respect to the state-of-the-art OMI NO₂ and HCHO retrievals using Bayesian data
762 fusion, as well as to unravel the intricacies of TOH to its key inputs such as tropospheric and stratospheric
763 ozone and water vapor.

764 We found large positive biases in tropospheric NO₂ columns in M2GMI, the archived model used as
765 an input to the parameterization of OH, compared to OMI over Africa, Eastern Europe, and the Midwest US.
766 Because of a large positive effect of NO₂ (a surrogate for NO_x) on TOH, a tendency well captured by our
767 implicit parameterization, these overestimations introduced significant regional biases in TOH up to 20%, and
768 a global overestimation of TOH by 1%. Consistent with former work, we saw distinct disparities in the sign
769 of linear trends of tropospheric NO₂ over high- and medium-income countries (i.e., negative) and low-income
770 countries (i.e., positive). While M2GMI generally replicated these trends, notable deviations were identified
771 over China leading to an erroneous trend of TOH.

772 Pronounced inaccuracies with regards to both the simulated HCHO magnitude and trend in M2GMI
773 were revealed by OMI over land. However, this proxy for OH was loosely connected to TOH in areas where
774 photolysis was not the major sink of HCHO (Wolfe et al., 2019), especially over land. Over oceans, where
775 HCHO and TOH were highly correlated, adjustments to M2GMI by OMI HCHO were relatively mild resulting
776 in small alterations to TOH which was by an order of magnitude lower than those of NO₂. These mild
777 alterations speak to either an insufficient amount of information in OMI or the reasonable accuracy of M2GMI
778 over pristine areas.

779 In general, five variables including NO₂, HCHO, water vapor, tropospheric ozone, and stratospheric
780 ozone, could collectively account for 65% of the variance in TOH trends globally. To estimate this, we
781 executed various modeling experiments to isolate the effect of NO₂, HCHO, water vapor, tropospheric ozone,
782 and stratospheric ozone on long-term trends of TOH in 2005-2019 at 1°×1° resolution. Except for tropospheric
783 ozone, these variables were either constrained by observations or aligned with independent observations,
784 boosting confidence in our trend results. Given the robust positive correlation between OH and NO₂, HCHO,
785 water vapor, and tropospheric ozone over regions where photochemistry was active, TOH trends influenced
786 by these variables closely mirrored the trends in their respective drivers/proxies. For instance, high- and
787 medium-income countries exhibited negative TOH trends driven by NO₂. Rising tropospheric ozone over east
788 and south Asia, heavily vetted by various observations (Guadel et al., 2018), led to an upswing in TOH over
789 the Pacific Ocean. The trend of water vapor, greatly in agreement with independent observation (Broger et al.,
790 2022), was dominantly positive over oceans leading to further enhancement of TOH. Rising HCHO over
791 Pacific and Indian Ocean suggested by constrained M2GMI was associated with increased TOH. The effect
792 of stratospheric ozone on TOH was marginal in low and mid latitudes due to negligible changes in stratospheric
793 ozone columns in M2GMI reconfirmed by OMI total ozone column observations.

794 A large offset between our analysis experiment with varying CO and CH₄ concentrations was observed
795 after removing the sum of the linear trends derived from these five key experiments from the analysis
796 experiment, indicating that our future research using ECCOH should include new experiments isolating the
797 effects of CO, CH₄, and transport (e.g., Gaubert et al., 2017; Zhao et al., 2020). Those experiments will refine
798 the investigation of the unexplained portion of the TOH trend.

799 The development of an effective parameterization of OH, that is capable of integrating advanced
800 satellite-based gas retrievals and improved weather forecast models enabled us to unravel the convoluted
801 response of TOH to various parameters. Nonetheless, it is important to recognize some of the limitations

802 associated with our work: first, the offline nature of the Bayesian data fusion algorithm makes the entire
803 experiment blind to the interconnected responses of various compounds, such as ozone or aerosols, to
804 adjustments to NO₂ and HCHO. Despite this limitation, our work has provided valuable insights into the first-
805 order effects of adjustments on TOH key inputs. This can help quickly identify areas where our prior
806 knowledge is least reliable to simulate TOH. Second, the machine learning algorithm employed for
807 parameterizing OH is implicit and its response to drivers/proxies is complex, making it difficult to
808 quantitatively verify against full chemistry models. However, by including a vast number of parameters in the
809 parameterization, Anderson et al. (2022) boosted its ability to understand the convoluted chemistry of OH.
810 This has allowed for reproducing OH for events not included in the training dataset (Anderson et al., 2022,
811 2023, 2024).

812 The longevity and stability of Aura's record of observations have played a significant role in
813 constraining/assessing several important variables pertaining to TOH on a global scale. This is exemplified by
814 the wealth of information obtained from OMI NO₂, HCHO, water vapor, total ozone columns, and Microwave
815 Limb Sounding (MLS) temperature and ozone, that are used directly or indirectly in our analysis. However,
816 as Aura's mission comes to an end, there will be a gap in the monitoring of these variables. TROPOMI, OMI's
817 successor, can help fill this gap, but its record of observation is still short; therefore, it is important to invest
818 in research to harmonize data from multiple satellite observations such as OMI and TROPOMI (e.g., Hilboll
819 et al., 2013). This is because each sensor can have different biases and spatial representativity, which can lead
820 to inconsistencies and potentially conflicting values if they are used together.

821 **Acknowledgements**

822 This research was supported by the National Aeronautics and Space Administration (NASA) Aura Mission
823 project science funds. We thank Gonzalo Gonzalez Abad for sharing OMI HCHO v4 data.

824 **Data availability**

825 Satellite data can be accessed for Level 2 OMI tropospheric NO₂ at
826 <https://doi.org/10.5067/MEASURES/MINDS/DATA204> (Lamsal et al., 2022), Level 2 OMI total ozone
827 columns at https://disc.gsfc.nasa.gov/datasets/OMTO3_003/summary (Bhartia, 2005), OMI SAO HCHO at
828 https://waps.cfa.harvard.edu/sao_atmos/data/omi_hcho/OMI-HCHO-L2/ (Gonzalez Abad, 2023), MOPITT
829 CO (https://doi.org/10.5067/TERRA/MOPITT/MOP03JM_L3.008) (NASA LARC, 2000), OMI/MLS TO₃
830 at https://acd-ext.gsfc.nasa.gov/Data_services/cloud_slice/data/tco_omimls.nc (Ziemke, 2023).

831 In-situ CO and CH₄ observations can be obtained from
832 <https://gml.noaa.gov/dv/data/index.php?category=Greenhouse%2BGases> (Helmig et al., 2021; Lan et
833 al., 2021).

834 MERRA2-GMI model outputs can be downloaded from [https://acd-
835 ext.gsfc.nasa.gov/Projects/GEOSCCM/MERRA2GMI/](https://acd-ext.gsfc.nasa.gov/Projects/GEOSCCM/MERRA2GMI/) (NASA Goddard Space Flight Center, 2023).

836 **Code availability**

837 OI-SAT-GMI python package developed for this research can be found from
838 <https://doi.org/10.5281/zenodo.10520136> (Souri, 2024).

839 GEOS-Quickchem used to run the modeling experiments encompassing ECCOH can be found from
840 <https://github.com/GEOS-ESM/QuickChem.git>.

841 GEOS model can be obtained from <https://github.com/GEOS-ESM/GEOSgcm.git>.

842 Offline ECCOH calculations to derive the sensitivity of TOH to different drivers/proxies can be obtained
843 from <https://doi.org/10.5281/zenodo.10685100>

844 **Authors contributions**

845 A.H.S and B.N.D designed the research. A.H.S analyzed the data, conducted the simulations, made all the
846 figures, and wrote the original manuscript. B.N.D helped with conceptualization, fund raising, and writing.
847 S.A.S helped configuring the model and interpreting the results. M.E.M and D.C.A implemented the improved
848 ECCOH module into GEOS-5 Quickchem. J.L. thoroughly validated the model with respect to CO and CH₄
849 observations. B.W. provided an improved CO emission inventory. L.D.O provided M2GMI and helped

850 interpret it. Z.Z. provided improved wetland CH₄ emissions. All the authors contributed to the discussion and
851 edited the paper.

852 **Competing interests**

853 B.N.D is a member of the editorial board of Atmospheric Chemistry and Physics.

854

855 **References**

856

857 Allan, R. P., Willett, K. M., John, V. O., and Trent, T.: Global Changes in Water Vapor 1979–2020, *J.*
858 *Geophys. Res. Atmos.*, 127, e2022JD036728, <https://doi.org/10.1029/2022JD036728>, 2022.

859 Anderson, D. C., Duncan, B. N., Fiore, A. M., Baublitz, C. B., Follette-Cook, M. B., Nicely, J. M., and Wolfe,
860 G. M.: Spatial and temporal variability in the hydroxyl (OH) radical: understanding the role of large-
861 scale climate features and their influence on OH through its dynamical and photochemical drivers,
862 *Atmos. Chem. Phys.*, 21, 6481–6508, <https://doi.org/10.5194/acp-21-6481-2021>, 2021.

863 Anderson, D. C., Duncan, B. N., Nicely, J. M., Liu, J., Strode, S. A., and Follette-Cook, M. B.: Technical note:
864 Constraining the hydroxyl (OH) radical in the tropics with satellite observations of its drivers – first
865 steps toward assessing the feasibility of a global observation strategy, *Atmos. Chem. Phys.*, 23, 6319–
866 6338, <https://doi.org/10.5194/acp-23-6319-2023>, 2023.

867 Anderson, D. C., Follette-Cook, M. B., Strode, S. A., Nicely, J. M., Liu, J., Ivatt, P. D., and Duncan, B. N.: A
868 machine learning methodology for the generation of a parameterization of the hydroxyl radical,
869 *Geosci. Model Dev.*, 15, 6341–6358, <https://doi.org/10.5194/gmd-15-6341-2022>, 2022.

870 Bacmeister, J. T., Suarez, M. J., and Robertson, F. R.: Rain Reevaporation, Boundary Layer–Convection
871 Interactions, and Pacific Rainfall Patterns in an AGCM, *J. Atmos. Sci.*, 63, 3383–3403,
872 <https://doi.org/10.1175/JAS3791.1>, 2006.

873 Baublitz, C. B., Fiore, A. M., Ludwig, S. M., Nicely, J. M., Wolfe, G. M., Murray, L. T., Commane, R., Prather,
874 M. J., Anderson, D. C., Correa, G., Duncan, B. N., Follette-Cook, M., Westervelt, D. M., Bourgeois,
875 I., Brune, W. H., Bui, T. P., DiGangi, J. P., Diskin, G. S., Hall, S. R., McKain, K., Miller, D. O.,
876 Peischl, J., Thames, A. B., Thompson, C. R., Ullmann, K., and Wofsy, S. C.: An observation-based,
877 reduced-form model for oxidation in the remote marine troposphere, *Proc. Natl. Acad. Sci.*, 120,
878 e2209735120, <https://doi.org/10.1073/pnas.2209735120>, 2023.

879 Bauwens, M., Stavrakou, T., Müller, J.-F., De Smedt, I., Van Roozendael, M., van der Werf, G. R.,
880 Wiedinmyer, C., Kaiser, J. W., Sindelarova, K., and Guenther, A.: Nine years of global hydrocarbon
881 emissions based on source inversion of OMI formaldehyde observations, *Atmos. Chem. Phys.*, 16,
882 10133–10158, <https://doi.org/10.5194/acp-16-10133-2016>, 2016.

883 Bauwens, M., Verreyken, B., Stavrakou, T., Müller, J.-F., and Smedt, I. D.: Spaceborne evidence for
884 significant anthropogenic VOC trends in Asian cities over 2005–2019, *Environ. Res. Lett.*, 17,
885 015008, <https://doi.org/10.1088/1748-9326/ac46eb>, 2022.

886 Bhartia, Pawan K., (2005), OMI/Aura Ozone (O3) Total Column 1-Orbit L2 Swath 13x24 km V003,
887 Greenbelt, MD, USA, Goddard Earth Sciences Data and Information Services Center (GES DISC),
888 Accessed: June 2023, 10.5067/Aura/OMI/DATA2024

889 Bocquet, M., Elbern, H., Eskes, H., Hirtl, M., Žabkar, R., Carmichael, G. R., Flemming, J., Inness, A.,
890 Pagowski, M., Pérez Camaño, J. L., Saide, P. E., San Jose, R., Sofiev, M., Vira, J., Baklanov, A.,
891 Carnevale, C., Grell, G., and Seigneur, C.: Data assimilation in atmospheric chemistry models: current
892 status and future prospects for coupled chemistry meteorology models, *Atmos. Chem. Phys.*, 15,
893 5325–5358, <https://doi.org/10.5194/acp-15-5325-2015>, 2015.

894 Borger, C., Beirle, S., and Wagner, T.: Analysis of global trends of total column water vapour from multiple
895 years of OMI observations, *Atmos. Chem. Phys.*, 22, 10603–10621, <https://doi.org/10.5194/acp-22-10603-2022>, 2022.

897 Bosilovich, M. G., Robertson, F. R., Takacs, L., Molod, A., and Mocko, D.: Atmospheric Water Balance and
898 Variability in the MERRA-2 Reanalysis, *J. Clim.*, 30, 1177–1196, <https://doi.org/10.1175/JCLI-D-16-0338.1>, 2017.

900 Bousquet, P., Hauglustaine, D. A., Peylin, P., Carouge, C., and Ciais, P.: Two decades of OH variability as
901 inferred by an inversion of atmospheric transport and chemistry of methyl chloroform, *Atmos. Chem.*
902 *Phys.*, 5, 2635–2656, <https://doi.org/10.5194/acp-5-2635-2005>, 2005.

903 Brune, W. H., Miller, D. O., Thames, A. B., Allen, H. M., Apel, E. C., Blake, D. R., Bui, T. P., Commane, R.,
904 Crounse, J. D., Daube, B. C., Diskin, G. S., DiGangi, J. P., Elkins, J. W., Hall, S. R., Hanisco, T. F.,

905 Hannun, R. A., Hintsä, E. J., Hornbrook, R. S., Kim, M. J., McKain, K., Moore, F. L., Neuman, J. A.,
906 Nicely, J. M., Peischl, J., Ryerson, T. B., St. Clair, J. M., Sweeney, C., Teng, A. P., Thompson, C.,
907 Ullmann, K., Veres, P. R., Wennberg, P. O., and Wolfe, G. M.: Exploring Oxidation in the Remote
908 Free Troposphere: Insights From Atmospheric Tomography (ATom), *J. Geophys. Res. Atmos.*, 125,
909 e2019JD031685, <https://doi.org/10.1029/2019JD031685>, 2020.

910 Brune, W. H., Miller, D. O., Thames, A. B., Brosius, A. L., Barletta, B., Blake, D. R., Blake, N. J., Chen, G.,
911 Choi, Y., Crawford, J. H., Digangi, J. P., Diskin, G., Fried, A., Hall, S. R., Hanisco, T. F., Huey, G.
912 L., Hughes, S. C., Kim, M., Meinardi, S., Montzka, D. D., Pusede, S. E., Schroeder, J. R., Teng, A.,
913 Tanner, D. J., Ullmann, K., Walega, J., Weinheimer, A., Wisthaler, A., and Wennberg, P. O.:
914 Observations of atmospheric oxidation and ozone production in South Korea, *Atmos. Environ.*, 269,
915 118854, <https://doi.org/10.1016/j.atmosenv.2021.118854>, 2022.

916 Canty, T. P., Hemberck, L., Vinciguerra, T. P., Anderson, D. C., Goldberg, D. L., Carpenter, S. F., Allen, D.
917 J., Loughner, C. P., Salawitch, R. J., and Dickerson, R. R.: Ozone and NO_x chemistry in the eastern
918 US: evaluation of CMAQ/CB05 with satellite (OMI) data, *Atmos. Chem. Phys.*, 15, 10965–10982,
919 <https://doi.org/10.5194/acp-15-10965-2015>, 2015.

920 Chen, B. and Liu, Z.: Global water vapor variability and trend from the latest 36 year (1979 to 2014) data of
921 ECMWF and NCEP reanalyses, radiosonde, GPS, and microwave satellite, *J. Geophys. Res. Atmos.*,
922 121, 11,442–11,462, <https://doi.org/10.1002/2016JD024917>, 2016.

923 Chin, M., Ginoux, P., Kinne, S., Torres, O., Holben, B. N., Duncan, B. N., Martin, R. V., Logan, J. A.,
924 Higurashi, A., and Nakajima, T.: Tropospheric Aerosol Optical Thickness from the GOCART Model
925 and Comparisons with Satellite and Sun Photometer Measurements, *J. Atmos. Sci.*, 59, 461–483,
926 [https://doi.org/10.1175/1520-0469\(2002\)059<0461:TAOTFT>2.0.CO;2](https://doi.org/10.1175/1520-0469(2002)059<0461:TAOTFT>2.0.CO;2), 2002.

927 Choi, S., Lamsal, L. N., Follette-Cook, M., Joiner, J., Krotkov, N. A., Swartz, W. H., Pickering, K. E.,
928 Loughner, C. P., Appel, W., Pfister, G., Saide, P. E., Cohen, R. C., Weinheimer, A. J., and Herman, J.
929 R.: Assessment of NO₂ observations during DISCOVER-AQ and KORUS-AQ field campaigns,
930 *Atmos. Meas. Tech.*, 13, 2523–2546, <https://doi.org/10.5194/amt-13-2523-2020>, 2020.

931 Choi, Y. and Souri, A. H.: Chemical condition and surface ozone in large cities of Texas during the last decade:
932 Observational evidence from OMI, CAMS, and model analysis, *Remote Sens. Environ.*, 168, 90–101,
933 <https://doi.org/10.1016/j.rse.2015.06.026>, 2015a.

934 Choi, Y. and Souri, A. H.: Seasonal behavior and long-term trends of tropospheric ozone, its precursors and
935 chemical conditions over Iran: A view from space, *Atmos. Environ.*, 106, 232–240,
936 <https://doi.org/10.1016/j.atmosenv.2015.02.012>, 2015b.

937 Chua, G., Naik, V., and Horowitz, L. W.: Exploring the drivers of tropospheric hydroxyl radical trends in the
938 Geophysical Fluid Dynamics Laboratory AM4.1 atmospheric chemistry–climate model, *Atmos.*
939 *Chem. Phys.*, 23, 4955–4975, <https://doi.org/10.5194/acp-23-4955-2023>, 2023.

940 Cox, C. and Munk, W.: Measurement of the Roughness of the Sea Surface from Photographs of the Sun's
941 Glitter, *J. Opt. Soc. Am., JOSA*, 44, 838–850, <https://doi.org/10.1364/JOSA.44.000838>, 1954.

942 Crippa, M., Guizzardi, D., Muntean, M., Schaaf, E., Vullo, E. L., Solazzo, E., Monforti-Ferrario, F., Olivier,
943 J., and Vignati, E.: EDGAR v5.0 Greenhouse Gas Emissions, 2019.

944 de Foy, B., Lu, Z., and Streets, D. G.: Satellite NO₂ retrievals suggest China has exceeded its NO_x reduction
945 goals from the twelfth Five-Year Plan, *Sci. Rep.*, 6, 35912, <https://doi.org/10.1038/srep35912>, 2016.

946 De Smedt, I., Stavroukou, T., Hendrick, F., Danckaert, T., Vlemmix, T., Pinardi, G., Theys, N., Lerot, C.,
947 Gielen, C., Vigouroux, C., Hermans, C., Fayt, C., Veeffkind, P., Müller, J.-F., and Van Roozendael,
948 M.: Diurnal, seasonal and long-term variations of global formaldehyde columns inferred from
949 combined OMI and GOME-2 observations, *Atmos. Chem. Phys.*, 15, 12519–12545,
950 <https://doi.org/10.5194/acp-15-12519-2015>, 2015.

951 Dhame, S., Taschetto, A. S., Santoso, A., and Meissner, K. J.: Indian Ocean warming modulates global
952 atmospheric circulation trends, *Clim. Dyn.*, 55, 2053–2073, <https://doi.org/10.1007/s00382-020-05369-1>, 2020.

954 Duncan, B. N., Lamsal, L. N., Thompson, A. M., Yoshida, Y., Lu, Z., Streets, D. G., Hurwitz, M. M., and
955 Pickering, K. E.: A space-based, high-resolution view of notable changes in urban NO_x pollution

956 around the world (2005–2014), *J. Geophys. Res. Atmos.*, 121, 976–996,
957 <https://doi.org/10.1002/2015JD024121>, 2016.

958 Duncan, B. N., Logan, J. A., Bey, I., Megretskaiia, I. A., Yantosca, R. M., Novelli, P. C., Jones, N. B., and
959 Rinsland, C. P.: Global budget of CO, 1988–1997: Source estimates and validation with a global
960 model, *J. Geophys. Res. Atmos.*, 112, <https://doi.org/10.1029/2007JD008459>, 2007b.

961 Duncan, B. N., Strahan, S. E., Yoshida, Y., Steenrod, S. D., and Livesey, N.: Model study of the cross-
962 tropopause transport of biomass burning pollution, *Atmos. Chem. Phys.*, 7, 3713–3736,
963 <https://doi.org/10.5194/acp-7-3713-2007>, 2007a.

964 Duncan, B. N., Yoshida, Y., Damon, M. R., Douglass, A. R., and Witte, J. C.: Temperature dependence of
965 factors controlling isoprene emissions, *Geophys. Res. Lett.*, 36,
966 <https://doi.org/10.1029/2008GL037090>, 2009.

967 Duncan, B., Portman, D., Bey, I., and Spivakovsky, C.: Parameterization of OH for efficient computation in
968 chemical tracer models, *J. Geophys. Res. Atmos.*, 105, 12259–12262,
969 <https://doi.org/10.1029/1999JD901141>, 2000.

970 Edwards, D. P., Lamarque, J.-F., Attié, J.-L., Emmons, L. K., Richter, A., Cammas, J.-P., Gille, J. C., Francis,
971 G. L., Deeter, M. N., Warner, J., Ziskin, D. C., Lyjak, L. V., Drummond, J. R., and Burrows, J. P.:
972 Tropospheric ozone over the tropical Atlantic: A satellite perspective, *J. Geophys. Res. Atmos.*, 108,
973 <https://doi.org/10.1029/2002JD002927>, 2003.

974 Elshorbany, Y. F., Duncan, B. N., Strobe, S. A., Wang, J. S., and Kouatchou, J.: The description and validation
975 of the computationally Efficient CH₄–CO–OH (ECCOHv1.01) chemistry module for 3-D model
976 applications, *Geosci. Model Dev.*, 9, 799–822, <https://doi.org/10.5194/gmd-9-799-2016>, 2016.

977 Fasnacht, Z., Vasilkov, A., Haffner, D., Qin, W., Joiner, J., Krotkov, N., Sayer, A. M., and Spurr, R.: A
978 geometry-dependent surface Lambertian-equivalent reflectivity product for UV–Vis retrievals – Part
979 2: Evaluation over open ocean, *Atmos. Meas. Tech.*, 12, 6749–6769, <https://doi.org/10.5194/amt-12-6749-2019>, 2019.

981 Ferrario, F. M., Crippa, M., Guizzardi, D., Muntean, M., Schaaf, E., Vullo, E. L., Solazzo, E., Olivier, J., and
982 Vignati, E.: EDGAR v6.0 Greenhouse Gas Emissions, 2021.

983 Fiore, A. M., Mickley, L. J., Zhu, Q., and Baublitz, C. B.: Climate and Tropospheric Oxidizing Capacity,
984 *Annu. Rev. Earth. Planet. Sci.*, 52, null, <https://doi.org/10.1146/annurev-earth-032320-090307>, 2024.

985 Gaubert, B., Worden, H. M., Arellano, A. F. J., Emmons, L. K., Tilmes, S., Barré, J., Martinez Alonso, S.,
986 Vitt, F., Anderson, J. L., Alkemade, F., Houweling, S., and Edwards, D. P.: Chemical Feedback From
987 Decreasing Carbon Monoxide Emissions, *Geophys. Res. Lett.*, 44, 9985–9995,
988 <https://doi.org/10.1002/2017GL074987>, 2017.

989 Gaudel, A., Cooper, O. R., Ancellet, G., Barret, B., Boynard, A., Burrows, J. P., Clerbaux, C., Coheur, P.-F.,
990 Cuesta, J., Cuevas, E., Doniki, S., Dufour, G., Ebojje, F., Foret, G., Garcia, O., Granados-Muñoz, M.
991 J., Hannigan, J. W., Hase, F., Hassler, B., Huang, G., Hurtmans, D., Jaffe, D., Jones, N., Kalabokas,
992 P., Kerridge, B., Kulawik, S., Latter, B., Leblanc, T., Le Flochmoën, E., Lin, W., Liu, J., Liu, X.,
993 Mahieu, E., McClure-Begley, A., Neu, J. L., Osman, M., Palm, M., Petetin, H., Petropavlovskikh, I.,
994 Querel, R., Rappoe, N., Rozanov, A., Schultz, M. G., Schwab, J., Siddans, R., Smale, D., Steinbacher,
995 M., Tanimoto, H., Tarasick, D. W., Thouret, V., Thompson, A. M., Trickl, T., Weatherhead, E.,
996 Wespes, C., Worden, H. M., Vigouroux, C., Xu, X., Zeng, G., and Ziemke, J.: Tropospheric Ozone
997 Assessment Report: Present-day distribution and trends of tropospheric ozone relevant to climate and
998 global atmospheric chemistry model evaluation, *Elem. Sci. Anth.*, 6, 39,
999 <https://doi.org/10.1525/elementa.291>, 2018.

1000 Gelaro, R., McCarty, W., Suárez, M. J., Todling, R., Molod, A., Takacs, L., Randles, C. A., Darmenov, A.,
1001 Bosilovich, M. G., Reichle, R., Wargan, K., Coy, L., Cullather, R., Draper, C., Akella, S., Buchard,
1002 V., Conaty, A., Silva, A. M. da, Gu, W., Kim, G.-K., Koster, R., Lucchesi, R., Merkova, D., Nielsen,
1003 J. E., Partyka, G., Pawson, S., Putman, W., Rienecker, M., Schubert, S. D., Sienkiewicz, M., and Zhao,
1004 B.: The Modern-Era Retrospective Analysis for Research and Applications, Version 2 (MERRA-2),
1005 *J. Clim.*, 30, 5419–5454, <https://doi.org/10.1175/JCLI-D-16-0758.1>, 2017.

1006 Giglio, L., Randerson, J. T., and van der Werf, G. R.: Analysis of daily, monthly, and annual burned area using
1007 the fourth-generation global fire emissions database (GFED4), *J. Geophys. Res. Biogeosci.*, 118, 317–
1008 328, <https://doi.org/10.1002/jgrg.20042>, 2013.

1009 Gonzalez Abad, (2003), OMI SAO HCHO Total Column L2 Swath V4, Cambridge, MA, USA, Accessed:
1010 May 2023, https://waps.cfa.harvard.edu/sao_atmos/data/omi_hcho/OMI-HCHO-L2/

1011 González Abad, G., Liu, X., Chance, K., Wang, H., Kurosu, T. P., and Suleiman, R.: Updated Smithsonian
1012 Astrophysical Observatory Ozone Monitoring Instrument (SAO OMI) formaldehyde retrieval, *Atmos.*
1013 *Meas. Tech.*, 8, 19–32, <https://doi.org/10.5194/amt-8-19-2015>, 2015.

1014 Hassler, B., McDonald, B. C., Frost, G. J., Borbon, A., Carslaw, D. C., Civerolo, K., Granier, C., Monks, P.
1015 S., Monks, S., Parrish, D. D., Pollack, I. B., Rosenlof, K. H., Ryerson, T. B., von Schneidmesser, E.,
1016 and Trainer, M.: Analysis of long-term observations of NO_x and CO in megacities and application to
1017 constraining emissions inventories, *Geophys. Res. Lett.*, 43, 9920–9930,
1018 <https://doi.org/10.1002/2016GL069894>, 2016.

1019 He, J., Naik, V., and Horowitz, L. W.: Hydroxyl Radical (OH) Response to Meteorological Forcing and
1020 Implication for the Methane Budget, *Geophys. Res. Lett.*, 48, e2021GL094140,
1021 <https://doi.org/10.1029/2021GL094140>, 2021.

1022 Helmig, D., Hueber, J., Tans, P., University Of Colorado Institute Of Arctic And Alpine Research
1023 (INSTAAR), & NOAA GML CCGG Group. (2021). University of Colorado Institute of Arctic and
1024 Alpine Research (INSTAAR) Flask-Air Sample Measurements of Atmospheric Non Methane
1025 Hydrocarbons Mole Fractions from the NOAA GML Carbon Cycle Surface Network at Global and
1026 Regional Background Sites, 2004-2016 (Version 2021.05.04) [Data set]. NOAA Global Monitoring
1027 Laboratory. <https://doi.org/10.15138/6AV8-GS57>

1028 Hickman, J. E., Andela, N., Tsigaridis, K., Galy-Lacaux, C., Ossouhou, M., and Bauer, S. E.: Reductions in
1029 NO₂ burden over north equatorial Africa from decline in biomass burning in spite of growing fossil
1030 fuel use, 2005 to 2017, *Proc. Natl. Acad. Sci.*, 118, e2002579118,
1031 <https://doi.org/10.1073/pnas.2002579118>, 2021.

1032 Hilboll, A., Richter, A., and Burrows, J. P.: Long-term changes of tropospheric NO₂ over megacities derived
1033 from multiple satellite instruments, *Atmos. Chem. Phys.*, 13, 4145–4169, <https://doi.org/10.5194/acp-13-4145-2013>, 2013.

1034 Holmes, C. D., Prather, M. J., Søvde, O. A., and Myhre, G.: Future methane, hydroxyl, and their uncertainties:
1035 key climate and emission parameters for future predictions, *Atmos. Chem. Phys.*, 13, 285–302,
1036 <https://doi.org/10.5194/acp-13-285-2013>, 2013.

1037 Hudman, R. C., Moore, N. E., Mebust, A. K., Martin, R. V., Russell, A. R., Valin, L. C., and Cohen, R. C.:
1038 Steps towards a mechanistic model of global soil nitric oxide emissions: implementation and space
1039 based-constraints, *Atmos. Chem. Phys.*, 12, 7779–7795, <https://doi.org/10.5194/acp-12-7779-2012>,
1040 2012.

1041 Jaeglé, L., Steinberger, L., V. Martin, R., and Chance, K.: Global partitioning of NO_x sources using satellite
1042 observations: Relative roles of fossil fuel combustion, biomass burning and soil emissions, *Faraday*
1043 *Discuss.*, 130, 407–423, <https://doi.org/10.1039/B502128F>, 2005.

1044 Jin, X. and Holloway, T.: Spatial and temporal variability of ozone sensitivity over China observed from the
1045 Ozone Monitoring Instrument, *J. Geophys. Res. Atmos.*, 120, 7229–7246,
1046 <https://doi.org/10.1002/2015JD023250>, 2015.

1047 Jones, M. W., Abatzoglou, J. T., Veraverbeke, S., Andela, N., Lasslop, G., Forkel, M., Smith, A. J. P., Burton,
1048 C., Betts, R. A., van der Werf, G. R., Sitch, S., Canadell, J. G., Santín, C., Kolden, C., Doerr, S. H.,
1049 and Le Quééré, C.: Global and Regional Trends and Drivers of Fire Under Climate Change, *Rev.*
1050 *Geophys.*, 60, e2020RG000726, <https://doi.org/10.1029/2020RG000726>, 2022.

1051 Jung, J., Souri, A. H., Wong, D. C., Lee, S., Jeon, W., Kim, J., and Choi, Y.: The Impact of the Direct Effect
1052 of Aerosols on Meteorology and Air Quality Using Aerosol Optical Depth Assimilation During the
1053 KORUS-AQ Campaign, *J. Geophys. Res. Atmos.*, 124, 8303–8319,
1054 <https://doi.org/10.1029/2019JD030641>, 2019.

1056 Krotkov, N. A., McLinden, C. A., Li, C., Lamsal, L. N., Celarier, E. A., Marchenko, S. V., Swartz, W. H.,
1057 Bucsela, E. J., Joiner, J., Duncan, B. N., Boersma, K. F., Veefkind, J. P., Levelt, P. F., Fioletov, V. E.,
1058 Dickerson, R. R., He, H., Lu, Z., and Streets, D. G.: Aura OMI observations of regional SO₂ and NO₂
1059 pollution changes from 2005 to 2015, *Atmos. Chem. Phys.*, 16, 4605–4629,
1060 <https://doi.org/10.5194/acp-16-4605-2016>, 2016.

1061 Kuttippurath, J., Abhishek, K., Gopikrishnan, G. S., and Pathak, M.: Investigation of long-term trends and
1062 major sources of atmospheric HCHO over India, *Environ. Chall.*, 7, 100477,
1063 <https://doi.org/10.1016/j.envc.2022.100477>, 2022.

1064 Kwon, H.-A., Abad, G. G., Nowlan, C. R., Chong, H., Souri, A. H., Vigouroux, C., Röhlings, A., Kivi, R.,
1065 Makarova, M., Notholt, J., Palm, M., Winkler, H., Té, Y., Sussmann, R., Rettinger, M., Mahieu, E.,
1066 Strong, K., Lutsch, E., Yamanouchi, S., Nagahama, T., Hannigan, J. W., Zhou, M., Murata, I., Grutter,
1067 M., Stremme, W., De Mazière, M., Jones, N., Smale, D., and Morino, I.: Validation of OMPS Suomi
1068 NPP and OMPS NOAA-20 Formaldehyde Total Columns With NDACC FTIR Observations, *Earth
1069 Space Sci.*, 10, e2022EA002778, <https://doi.org/10.1029/2022EA002778>, 2023.

1070 Lamsal, L. N., Duncan, B. N., Yoshida, Y., Krotkov, N. A., Pickering, K. E., Streets, D. G., and Lu, Z.: U.S.
1071 NO₂ trends (2005–2013): EPA Air Quality System (AQS) data versus improved observations from
1072 the Ozone Monitoring Instrument (OMI), *Atmos. Environ.*, 110, 130–143,
1073 <https://doi.org/10.1016/j.atmosenv.2015.03.055>, 2015.

1074 Lamsal, L. N., Krotkov, N. A., Vasilkov, A., Marchenko, S., Qin, W., Yang, E.-S., Fasnacht, Z., Joiner, J.,
1075 Choi, S., Haffner, D., Swartz, W. H., Fisher, B., and Bucsela, E.: Ozone Monitoring Instrument (OMI)
1076 Aura nitrogen dioxide standard product version 4.0 with improved surface and cloud treatments,
1077 *Atmos. Meas. Tech.*, 14, 455–479, <https://doi.org/10.5194/amt-14-455-2021>, 2021.

1078 Lamsal, Lok N., Nikolay A. Krotkov, Sergey V. Marchenko, Joanna Joiner, Luke Oman, Alexander Vasilkov,
1079 Bradford Fisher, Wenhan Qin, Eun-Su Yang, Zachary Fasnacht, Sungyeon Choi, Peter Leonard, and
1080 David Haffner (2022), OMI/Aura NO₂ Tropospheric, Stratospheric & Total Columns MINDS 1-Orbit
1081 L2 Swath 13 kmx24 km, NASA Goddard Space Flight Center, Goddard Earth Sciences Data and
1082 Information Services Center (GES DISC), Accessed: May 2023,
1083 10.5067/MEASURES/MINDS/DATA204

1084 Lan, X., J.W. Mund, A.M. Crotwell, M.J. Crotwell, E. Moglia, M. Madronich, D. Neff and K.W. Thoning
1085 (2023), Atmospheric Methane Dry Air Mole Fractions from the NOAA GML Carbon Cycle
1086 Cooperative Global Air Sampling Network, 1983-2022, Version: 2023-08-28,
1087 <https://doi.org/10.15138/VNCZ-M766>

1088 Lawrence, M. G., Jöckel, P., and von Kuhlmann, R.: What does the global mean OH concentration tell us?,
1089 *Atmos. Chem. Phys.*, 1, 37–49, <https://doi.org/10.5194/acp-1-37-2001>, 2001.

1090 Lelieveld, J., Gromov, S., Pozzer, A., and Taraborrelli, D.: Global tropospheric hydroxyl distribution, budget
1091 and reactivity, *Atmos. Chem. Phys.*, 16, 12477–12493, <https://doi.org/10.5194/acp-16-12477-2016>,
1092 2016.

1093 Lin, M., Horowitz, L. W., Payton, R., Fiore, A. M., and Tonnesen, G.: US surface ozone trends and extremes
1094 from 1980 to 2014: quantifying the roles of rising Asian emissions, domestic controls, wildfires, and
1095 climate, *Atmos. Chem. Phys.*, 17, 2943–2970, <https://doi.org/10.5194/acp-17-2943-2017>, 2017.

1096 Marais, E. A., Jacob, D. J., Kurosu, T. P., Chance, K., Murphy, J. G., Reeves, C., Mills, G., Casadio, S., Millet,
1097 D. B., Barkley, M. P., Paulot, F., and Mao, J.: Isoprene emissions in Africa inferred from OMI
1098 observations of formaldehyde columns, *Atmos. Chem. Phys.*, 12, 6219–6235,
1099 <https://doi.org/10.5194/acp-12-6219-2012>, 2012.

1100 Marquardt, D. W.: An Algorithm for Least-Squares Estimation of Nonlinear Parameters, *J. Soc. Indust. Appl.
1101 Math.*, 11, 431–441, <https://doi.org/10.1137/0111030>, 1963.

1102 Miller, D. O. and Brune, W. H.: Investigating the Understanding of Oxidation Chemistry Using 20 Years of
1103 Airborne OH and HO₂ Observations, *J. Geophys. Res. Atmos.*, 127, e2021JD035368,
1104 <https://doi.org/10.1029/2021JD035368>, 2022.

1105 Millet, D. B., Jacob, D. J., Boersma, K. F., Fu, T.-M., Kurosu, T. P., Chance, K., Heald, C. L., and Guenther,
1106 A.: Spatial distribution of isoprene emissions from North America derived from formaldehyde column

1107 measurements by the OMI satellite sensor, *J. Geophys. Res. Atmos.*, 113,
 1108 <https://doi.org/10.1029/2007JD008950>, 2008.
 1109 Miyazaki, K., Bowman, K. W., Yumimoto, K., Walker, T., and Sudo, K.: Evaluation of a multi-model, multi-
 1110 constituent assimilation framework for tropospheric chemical reanalysis, *Atmos. Chem. Phys.*, 20,
 1111 931–967, <https://doi.org/10.5194/acp-20-931-2020>, 2020.
 1112 Molod, A., Takacs, L., Suarez, M., and Bacmeister, J.: Development of the GEOS-5 atmospheric general
 1113 circulation model: evolution from MERRA to MERRA2, *Geosci. Model Dev.*, 8, 1339–1356,
 1114 <https://doi.org/10.5194/gmd-8-1339-2015>, 2015.
 1115 Moorthi, S. and Suarez, M. J.: Relaxed Arakawa-Schubert. A Parameterization of Moist Convection for
 1116 General Circulation Models, *Mon. Weather Rev.*, 120, 978–1002, [https://doi.org/10.1175/1520-0493\(1992\)120<0978:RASAPO>2.0.CO;2](https://doi.org/10.1175/1520-0493(1992)120<0978:RASAPO>2.0.CO;2), 1992.
 1117 Murray, L. T., Fiore, A. M., Shindell, D. T., Naik, V., and Horowitz, L. W.: Large uncertainties in global
 1118 hydroxyl projections tied to fate of reactive nitrogen and carbon, *Proc. Natl. Acad. Sci.*, 118,
 1119 e2115204118, <https://doi.org/10.1073/pnas.2115204118>, 2021.
 1120 Murray, L. T., Logan, J. A., and Jacob, D. J.: Interannual variability in tropical tropospheric ozone and OH:
 1121 The role of lightning, *J. Geophys. Res. Atmos.*, 118, 11,468–11,480,
 1122 <https://doi.org/10.1002/jgrd.50857>, 2013.
 1123 Naik, V., Voulgarakis, A., Fiore, A. M., Horowitz, L. W., Lamarque, J.-F., Lin, M., Prather, M. J., Young, P.
 1124 J., Bergmann, D., Cameron-Smith, P. J., Cionni, I., Collins, W. J., Dalsøren, S. B., Doherty, R., Eyring,
 1125 V., Faluvegi, G., Folberth, G. A., Josse, B., Lee, Y. H., MacKenzie, I. A., Nagashima, T., van Noije,
 1126 T. P. C., Plummer, D. A., Righi, M., Rumbold, S. T., Skeie, R., Shindell, D. T., Stevenson, D. S.,
 1127 Strode, S., Sudo, K., Szopa, S., and Zeng, G.: Preindustrial to present-day changes in tropospheric
 1128 hydroxyl radical and methane lifetime from the Atmospheric Chemistry and Climate Model
 1129 Intercomparison Project (ACCMIP), *Atmos. Chem. Phys.*, 13, 5277–5298,
 1130 <https://doi.org/10.5194/acp-13-5277-2013>, 2013.
 1131 Naimark, J. G., Fiore, A. M., Jin, X., Wang, Y., Klovenski, E., and Braneon, C.: Evaluating Drought Responses
 1132 of Surface Ozone Precursor Proxies: Variations With Land Cover Type, Precipitation, and
 1133 Temperature, *Geophys. Res. Lett.*, 48, e2020GL091520, <https://doi.org/10.1029/2020GL091520>,
 1134 2021.
 1135 NASA Goddard Space Flight Center: MERRA2 GMI, NASA, [https://acd-445
 1136 ext.gsfc.nasa.gov/Projects/GEOSCCM/MERRA2GMI/](https://acd-445.ext.gsfc.nasa.gov/Projects/GEOSCCM/MERRA2GMI/), last access: 12 Feb. 2023.
 1137 NASA LARC. (2000) MOPITT CO gridded monthly means (Near and Thermal Infrared Radiances) V008,
 1138 NASA Langley Atmospheric Science Data Center DAAC,
 1139 https://doi.org/10.5067/TERRA/MOPITT/MOP03JM_L3.008
 1140 Naus, S., Montzka, S. A., Pandey, S., Basu, S., Dlugokencky, E. J., and Krol, M.: Constraints and biases in a
 1141 tropospheric two-box model of OH, *Atmos. Chem. Phys.*, 19, 407–424, [https://doi.org/10.5194/acp-
 1142 19-407-2019](https://doi.org/10.5194/acp-19-407-2019), 2019.
 1143 Nguyen, N. H., Turner, A. J., Yin, Y., Prather, M. J., and Frankenberg, C.: Effects of Chemical Feedbacks on
 1144 Decadal Methane Emissions Estimates, *Geophys. Res. Lett.*, 47, e2019GL085706,
 1145 <https://doi.org/10.1029/2019GL085706>, 2020.
 1146 Nicely, J. M., Canty, T. P., Manyin, M., Oman, L. D., Salawitch, R. J., Steenrod, S. D., Strahan, S. E., and
 1147 Strode, S. A.: Changes in Global Tropospheric OH Expected as a Result of Climate Change Over the
 1148 Last Several Decades, *J. Geophys. Res. Atmos.*, 123, 10,774–10,795,
 1149 <https://doi.org/10.1029/2018JD028388>, 2018.
 1150 Nicely, J. M., Duncan, B. N., Hanisco, T. F., Wolfe, G. M., Salawitch, R. J., Deushi, M., Haslerud, A. S.,
 1151 Jöckel, P., Josse, B., Kinnison, D. E., Klekociuk, A., Manyin, M. E., Marécal, V., Morgenstern, O.,
 1152 Murray, L. T., Myhre, G., Oman, L. D., Pitari, G., Pozzer, A., Quaglia, I., Revell, L. E., Rozanov, E.,
 1153 Stenke, A., Stone, K., Strahan, S., Tilmes, S., Tost, H., Westervelt, D. M., and Zeng, G.: A machine
 1154 learning examination of hydroxyl radical differences among model simulations for CCMI-1, *Atmos.
 1155 Chem. Phys.*, 20, 1341–1361, <https://doi.org/10.5194/acp-20-1341-2020>, 2020.
 1156

1157 Nielsen, J. E., Pawson, S., Molod, A., Auer, B., da Silva, A. M., Douglass, A. R., Duncan, B., Liang, Q.,
1158 Manyin, M., Oman, L. D., Putman, W., Strahan, S. E., and Wargan, K.: Chemical Mechanisms and
1159 Their Applications in the Goddard Earth Observing System (GEOS) Earth System Model, *J. Adv.*
1160 *Model. Earth Syst.*, 9, 3019–3044, <https://doi.org/10.1002/2017MS001011>, 2017.

1161 Nowlan, C. R., González Abad, G., Kwon, H.-A., Ayazpour, Z., Chan Miller, C., Chance, K., Chong, H., Liu,
1162 X., O’Sullivan, E., Wang, H., Zhu, L., De Smedt, I., Jaross, G., Seftor, C., and Sun, K.: Global
1163 Formaldehyde Products From the Ozone Mapping and Profiler Suite (OMPS) Nadir Mappers on
1164 Suomi NPP and NOAA-20, *Earth Space Sci.*, 10, e2022EA002643,
1165 <https://doi.org/10.1029/2022EA002643>, 2023.

1166 Orbe, C., Oman, L. D., Strahan, S. E., Waugh, D. W., Pawson, S., Takacs, L. L., and Molod, A. M.: Large-
1167 Scale Atmospheric Transport in GEOS Replay Simulations, *J. Adv. Model. Earth Syst.*, 9, 2545–2560,
1168 <https://doi.org/10.1002/2017MS001053>, 2017.

1169 Parrish, D. F. and Derber, J. C.: The National Meteorological Center’s Spectral Statistical-Interpolation
1170 Analysis System, *Mon. Weather Rev.*, 120, 1747–1763, [https://doi.org/10.1175/1520-0493\(1992\)120<1747:TNMCSS>2.0.CO;2](https://doi.org/10.1175/1520-0493(1992)120<1747:TNMCSS>2.0.CO;2), 1992.

1172 Patra, P. K., Krol, M. C., Montzka, S. A., Arnold, T., Atlas, E. L., Lintner, B. R., Stephens, B. B., Xiang, B.,
1173 Elkins, J. W., Fraser, P. J., Ghosh, A., Hints, E. J., Hurst, D. F., Ishijima, K., Krummel, P. B., Miller,
1174 B. R., Miyazaki, K., Moore, F. L., Mühle, J., O’Doherty, S., Prinn, R. G., Steele, L. P., Takigawa, M.,
1175 Wang, H. J., Weiss, R. F., Wofsy, S. C., and Young, D.: Observational evidence for interhemispheric
1176 hydroxyl-radical parity, *Nature*, 513, 219–223, <https://doi.org/10.1038/nature13721>, 2014.

1177 Pinardi, G., Van Roozendaal, M., Hendrick, F., Theys, N., Abuhassan, N., Bais, A., Boersma, F., Cede, A.,
1178 Chong, J., Donner, S., Drosoglou, T., Dzhola, A., Eskes, H., Frieß, U., Granville, J., Herman, J. R.,
1179 Holla, R., Hovila, J., Irie, H., Kanaya, Y., Karagkiozidis, D., Kouremeti, N., Lambert, J.-C., Ma, J.,
1180 Peters, E., PETERS, A., Postlyakov, O., Richter, A., Remmers, J., Takashima, H., Tiefengraber, M.,
1181 Valks, P., Vlemmix, T., Wagner, T., and Wittrock, F.: Validation of tropospheric NO₂ column
1182 measurements of GOME-2A and OMI using MAX-DOAS and direct sun network observations,
1183 *Atmos. Meas. Tech.*, 13, 6141–6174, <https://doi.org/10.5194/amt-13-6141-2020>, 2020.

1184 Qin, W., Fasnacht, Z., Haffner, D., Vasilkov, A., Joiner, J., Krotkov, N., Fisher, B., and Spurr, R.: A geometry-
1185 dependent surface Lambertian-equivalent reflectivity product for UV–Vis retrievals – Part 1:
1186 Evaluation over land surfaces using measurements from OMI at 466 nm, *Atmos. Meas. Tech.*, 12,
1187 3997–4017, <https://doi.org/10.5194/amt-12-3997-2019>, 2019.

1188 Ren, X., Olson, J. R., Crawford, J. H., Brune, W. H., Mao, J., Long, R. B., Chen, Z., Chen, G., Avery, M. A.,
1189 Sachse, G. W., Barrick, J. D., Diskin, G. S., Huey, L. G., Fried, A., Cohen, R. C., Heikes, B.,
1190 Wennberg, P. O., Singh, H. B., Blake, D. R., and Shetter, R. E.: HO_x chemistry during INTEX-A
1191 2004: Observation, model calculation, and comparison with previous studies, *J. Geophys. Res. Atmos.*,
1192 113, <https://doi.org/10.1029/2007JD009166>, 2008.

1193 Reuter, M., Buchwitz, M., Hilboll, A., Richter, A., Schneising, O., Hilker, M., Heymann, J., Bovensmann, H.,
1194 and Burrows, J. P.: Decreasing emissions of NO_x relative to CO₂ in East Asia inferred from satellite
1195 observations, *Nature Geosci.*, 7, 792–795, <https://doi.org/10.1038/ngeo2257>, 2014.

1196 Rigby, M., Montzka, S. A., Prinn, R. G., White, J. W. C., Young, D., O’Doherty, S., Lunt, M. F., Ganesan, A.,
1197 L., Manning, A. J., Simmonds, P. G., Salameh, P. K., Harth, C. M., Mühle, J., Weiss, R. F., Fraser, P.
1198 J., Steele, L. P., Krummel, P. B., McCulloch, A., and Park, S.: Role of atmospheric oxidation in recent
1199 methane growth, *Proc. Natl. Acad. Sci.*, 114, 5373–5377, <https://doi.org/10.1073/pnas.1616426114>,
1200 2017.

1201 Rodgers, C. D.: *Inverse Methods for Atmospheric Sounding: Theory and Practice*, WORLD SCIENTIFIC,
1202 Oxford, 2000.

1203 Sandu, A. and Chai, T.: Chemical Data Assimilation—An Overview, *Atm.*, 2, 426–463,
1204 <https://doi.org/10.3390/atmos2030426>, 2011.

1205 Saunois, M., Stavert, A. R., Poulter, B., Bousquet, P., Canadell, J. G., Jackson, R. B., Raymond, P. A.,
1206 Dlugokencky, E. J., Houweling, S., Patra, P. K., Ciais, P., Arora, V. K., Bastviken, D., Bergamaschi,
1207 P., Blake, D. R., Brailsford, G., Bruhwiler, L., Carlson, K. M., Carrol, M., Castaldi, S., Chandra, N.,

1208 Crevoisier, C., Crill, P. M., Covey, K., Curry, C. L., Etiopie, G., Frankenberg, C., Gedney, N., Hegglin,
1209 M. I., Höglund-Isaksson, L., Hugelius, G., Ishizawa, M., Ito, A., Janssens-Maenhout, G., Jensen, K.
1210 M., Joos, F., Kleinen, T., Krummel, P. B., Langenfelds, R. L., Laruelle, G. G., Liu, L., Machida, T.,
1211 Maksyutov, S., McDonald, K. C., McNorton, J., Miller, P. A., Melton, J. R., Morino, I., Müller, J.,
1212 Murguia-Flores, F., Naik, V., Niwa, Y., Noce, S., O'Doherty, S., Parker, R. J., Peng, C., Peng, S.,
1213 Peters, G. P., Prigent, C., Prinn, R., Ramonet, M., Regnier, P., Riley, W. J., Rosentreter, J. A., Segers,
1214 A., Simpson, I. J., Shi, H., Smith, S. J., Steele, L. P., Thornton, B. F., Tian, H., Tohjima, Y., Tubiello,
1215 F. N., Tsuruta, A., Viovy, N., Voulgarakis, A., Weber, T. S., van Weele, M., van der Werf, G. R.,
1216 Weiss, R. F., Worthy, D., Wunch, D., Yin, Y., Yoshida, Y., Zhang, W., Zhang, Z., Zhao, Y., Zheng,
1217 B., Zhu, Q., Zhu, Q., and Zhuang, Q.: The Global Methane Budget 2000–2017, *Earth Syst. Sci. Data.*,
1218 12, 1561–1623, <https://doi.org/10.5194/essd-12-1561-2020>, 2020.

1219 Shen, L., Jacob, D. J., Zhu, L., Zhang, Q., Zheng, B., Sulprizio, M. P., Li, K., De Smedt, I., González Abad,
1220 G., Cao, H., Fu, T.-M., and Liao, H.: The 2005–2016 Trends of Formaldehyde Columns Over China
1221 Observed by Satellites: Increasing Anthropogenic Emissions of Volatile Organic Compounds and
1222 Decreasing Agricultural Fire Emissions, *Geophys. Res. Lett.*, 46, 4468–4475,
1223 <https://doi.org/10.1029/2019GL082172>, 2019.

1224 Souri, A. H., Chance, K., Bak, J., Nowlan, C. R., González Abad, G., Jung, Y., Wong, D. C., Mao, J., and Liu,
1225 X.: Unraveling pathways of elevated ozone induced by the 2020 lockdown in Europe by an
1226 observationally constrained regional model using TROPOMI, *Atmos. Chem. Phys.*, 21, 18227–18245,
1227 <https://doi.org/10.5194/acp-21-18227-2021>, 2021.

1228 Souri, A. H., Choi, Y., Jeon, W., Li, X., Pan, S., Diao, L., and Westenbarger, D. A.: Constraining NO_x
1229 emissions using satellite NO₂ measurements during 2013 DISCOVER-AQ Texas campaign, *Atmos.*
1230 *Environ.*, 131, 371–381, <https://doi.org/10.1016/j.atmosenv.2016.02.020>, 2016.

1231 Souri, A. H., Choi, Y., Jeon, W., Woo, J.-H., Zhang, Q., and Kurokawa, J.: Remote sensing evidence of decadal
1232 changes in major tropospheric ozone precursors over East Asia, *J. Geophys. Res. Atmos.*, 122, 2474–
1233 2492, <https://doi.org/10.1002/2016JD025663>, 2017.

1234 Souri, A. H., Choi, Y., Kodros, J. K., Jung, J., Shpund, J., Pierce, J. R., Lynn, B. H., Khain, A., and Chance,
1235 K.: Response of Hurricane Harvey's rainfall to anthropogenic aerosols: A sensitivity study based on
1236 spectral bin microphysics with simulated aerosols, *Atmos. Res.*, 242, 104965,
1237 <https://doi.org/10.1016/j.atmosres.2020.104965>, 2020b.

1238 Souri, A. H., Johnson, M. S., Wolfe, G. M., Crawford, J. H., Fried, A., Wisthaler, A., Brune, W. H., Blake, D.
1239 R., Weinheimer, A. J., Verhoelst, T., Compernelle, S., Pinardi, G., Vigouroux, C., Langerock, B.,
1240 Choi, S., Lamsal, L., Zhu, L., Sun, S., Cohen, R. C., Min, K.-E., Cho, C., Philip, S., Liu, X., and
1241 Chance, K.: Characterization of errors in satellite-based HCHO  NO₂ tropospheric
1242 column ratios with respect to chemistry, column-to-PBL translation, spatial representation, and
1243 retrieval uncertainties, *Atmos. Chem. Phys.*, 23, 1963–1986, [https://doi.org/10.5194/acp-23-1963-](https://doi.org/10.5194/acp-23-1963-2023)
1244 2023, 2023.

1245 Souri, A. H., Nowlan, C. R., González Abad, G., Zhu, L., Blake, D. R., Fried, A., Weinheimer, A. J., Wisthaler,
1246 A., Woo, J.-H., Zhang, Q., Chan Miller, C. E., Liu, X., and Chance, K.: An inversion of NO_x and non-
1247 methane volatile organic compound (NMVOC) emissions using satellite observations during the
1248 KORUS-AQ campaign and implications for surface ozone over East Asia, *Atmos. Chem. Phys.*, 20,
1249 9837–9854, <https://doi.org/10.5194/acp-20-9837-2020>, 2020a.

1250 Souri, A. H., Nowlan, C. R., Wolfe, G. M., Lamsal, L. N., Chan Miller, C. E., Abad, G. G., Janz, S. J., Fried,
1251 A., Blake, D. R., Weinheimer, A. J., Diskin, G. S., Liu, X., and Chance, K.: Revisiting the effectiveness
1252 of HCHO/NO₂ ratios for inferring ozone sensitivity to its precursors using high resolution airborne
1253 remote sensing observations in a high ozone episode during the KORUS-AQ campaign, *Atmos.*
1254 *Environ.*, 224, 117341, <https://doi.org/10.1016/j.atmosenv.2020.117341>, 2020c.

1255 Souri, A. H., OI-SAT-GMI (0.1.0). Zenodo. <https://doi.org/10.5281/zenodo.10520136>, 2024

1256 Spivakovsky, C. M., Logan, J. A., Montzka, S. A., Balkanski, Y. J., Foreman-Fowler, M., Jones, D. B. A.,
1257 Horowitz, L. W., Fusco, A. C., Brenninkmeijer, C. a. M., Prather, M. J., Wofsy, S. C., and McElroy,

1258 M. B.: Three-dimensional climatological distribution of tropospheric OH: Update and evaluation, *J.*
1259 *Geophys. Res. Atmos.*, 105, 8931–8980, <https://doi.org/10.1029/1999JD901006>, 2000.

1260 Stavrakou, T., Müller, J.-F., De Smedt, I., Van Roozendael, M., van der Werf, G. R., Giglio, L., and Guenther,
1261 A.: Global emissions of non-methane hydrocarbons deduced from SCIAMACHY formaldehyde
1262 columns through 2003–2006, *Atmos. Chem. Phys.*, 9, 3663–3679, [https://doi.org/10.5194/acp-9-](https://doi.org/10.5194/acp-9-3663-2009)
1263 3663-2009, 2009.

1264 Strode, S. A., Duncan, B. N., Yegorova, E. A., Kouatchou, J., Ziemke, J. R., and Douglass, A. R.: Implications
1265 of carbon monoxide bias for methane lifetime and atmospheric composition in chemistry climate
1266 models, *Atmos. Chem. Phys.*, 15, 11789–11805, <https://doi.org/10.5194/acp-15-11789-2015>, 2015.

1267 Strode, S. A., Wang, J. S., Manyin, M., Duncan, B., Hossaini, R., Keller, C. A., Michel, S. E., and White, J.
1268 W. C.: Strong sensitivity of the isotopic composition of methane to the plausible range of tropospheric
1269 chlorine, *Atmos. Chem. Phys.*, 20, 8405–8419, <https://doi.org/10.5194/acp-20-8405-2020>, 2020.

1270 Strode, S. A., Ziemke, J. R., Oman, L. D., Lamsal, L. N., Olsen, M. A., and Liu, J.: Global changes in the
1271 diurnal cycle of surface ozone, *Atmos. Environ.*, 199, 323–333,
1272 <https://doi.org/10.1016/j.atmosenv.2018.11.028>, 2019.

1273 Thompson, A. M., Stauffer, R. M., Wargan, K., Witte, J. C., Kollonige, D. E., and Ziemke, J. R.: Regional and
1274 Seasonal Trends in Tropical Ozone From SHADOZ Profiles: Reference for Models and Satellite
1275 Products, *J. Geophys. Res. Atmos.*, 126, e2021JD034691, <https://doi.org/10.1029/2021JD034691>,
1276 2021.

1277 Trenberth, K. E., Fasullo, J., and Smith, L.: Trends and variability in column-integrated atmospheric water
1278 vapor, *Clim. Dyn.*, 24, 741–758, <https://doi.org/10.1007/s00382-005-0017-4>, 2005.

1279 Turner, A. J., Frankenberg, C., Wennberg, P. O., and Jacob, D. J.: Ambiguity in the causes for decadal trends
1280 in atmospheric methane and hydroxyl, *Proc. Natl. Acad. Sci.*, 114, 5367–5372,
1281 <https://doi.org/10.1073/pnas.1616020114>, 2017.

1282 Valin, L. C., Fiore, A. M., Chance, K., and González Abad, G.: The role of OH production in interpreting the
1283 variability of CH₂O columns in the southeast U.S., *J. Geophys. Res. Atmos.*, 121, 478–493,
1284 <https://doi.org/10.1002/2015JD024012>, 2016.

1285 van Marle, M. J. E., Kloster, S., Magi, B. I., Marlon, J. R., Daniau, A.-L., Field, R. D., Arneeth, A., Forrest, M.,
1286 Hantson, S., Kehrwald, N. M., Knorr, W., Lasslop, G., Li, F., Mangeon, S., Yue, C., Kaiser, J. W.,
1287 and van der Werf, G. R.: Historic global biomass burning emissions for CMIP6 (BB4CMIP) based on
1288 merging satellite observations with proxies and fire models (1750–2015), *Geosci. Model Dev.*, 10,
1289 3329–3357, <https://doi.org/10.5194/gmd-10-3329-2017>, 2017.

1290 Vinken, G. C. M., Boersma, K. F., Maasackers, J. D., Adon, M., and Martin, R. V.: Worldwide biogenic soil
1291 NO_x emissions inferred from OMI NO₂ observations, *Atmos. Chem. Phys.*, 14, 10363–10381,
1292 <https://doi.org/10.5194/acp-14-10363-2014>, 2014.

1293 Wang, R. and Liu, Y.: Recent declines in global water vapor from MODIS products: Artifact or real trend?,
1294 *Remote Sens. Environ.*, 247, 111896, <https://doi.org/10.1016/j.rse.2020.111896>, 2020.

1295 Wang, Y., Lin, N., Li, W., Guenther, A., Lam, J. C. Y., Tai, A. P. K., Potosnak, M. J., and Seco, R.: Satellite-
1296 derived constraints on the effect of drought stress on biogenic isoprene emissions in the southeastern
1297 US, *Atmos. Chem. Phys.*, 22, 14189–14208, <https://doi.org/10.5194/acp-22-14189-2022>, 2022.

1298 Wolfe, G. M., Nicely, J. M., St. Clair, J. M., Hanisco, T. F., Liao, J., Oman, L. D., Brune, W. B., Miller, D.,
1299 Thames, A., González Abad, G., Ryerson, T. B., Thompson, C. R., Peischl, J., McKain, K., Sweeney,
1300 C., Wennberg, P. O., Kim, M., Crounse, J. D., Hall, S. R., Ullmann, K., Diskin, G., Bui, P., Chang,
1301 C., and Dean-Day, J.: Mapping hydroxyl variability throughout the global remote troposphere via
1302 synthesis of airborne and satellite formaldehyde observations, *Proc. Natl. Acad. Sci.*, 116, 11171–
1303 11180, <https://doi.org/10.1073/pnas.1821661116>, 2019.

1304 Yienger, J. J. and Levy II, H.: Empirical model of global soil-biogenic NO_x emissions, *J. Geophys. Res.*
1305 *Atmos.*, 100, 11447–11464, <https://doi.org/10.1029/95JD00370>, 1995.

1306 Zhang, Q., He, K., and Huo, H.: Cleaning China’s air, *Nature*, 484, 161–162, <https://doi.org/10.1038/484161a>,
1307 2012.

1308 Zhang, Z., Poulter, B., Feldman, A. F., Ying, Q., Ciais, P., Peng, S., and Li, X.: Recent intensification of
1309 wetland methane feedback, *Nat. Clim. Chang.*, 13, 430–433, [https://doi.org/10.1038/s41558-023-](https://doi.org/10.1038/s41558-023-01629-0)
1310 01629-0, 2023.

1311 Zhang, Z., Zimmermann, N. E., Kaplan, J. O., and Poulter, B.: Modeling spatiotemporal dynamics of global
1312 wetlands: comprehensive evaluation of a new sub-grid TOPMODEL parameterization and
1313 uncertainties, *Biogeosciences*, 13, 1387–1408, <https://doi.org/10.5194/bg-13-1387-2016>, 2016.

1314 Zhao, Y., Saunois, M., Bousquet, P., Lin, X., Berchet, A., Hegglin, M. I., Canadell, J. G., Jackson, R. B.,
1315 Hauglustaine, D. A., Szopa, S., Stavert, A. R., Abraham, N. L., Archibald, A. T., Bekki, S., Deushi,
1316 M., Jöckel, P., Josse, B., Kinnison, D., Kirner, O., Marécal, V., O’Connor, F. M., Plummer, D. A.,
1317 Revell, L. E., Rozanov, E., Stenke, A., Strode, S., Tilmes, S., Dlugokencky, E. J., and Zheng, B.: Inter-
1318 model comparison of global hydroxyl radical (OH) distributions and their impact on atmospheric
1319 methane over the 2000–2016 period, *Atmos. Chem. Phys.*, 19, 13701–13723,
1320 <https://doi.org/10.5194/acp-19-13701-2019>, 2019.

1321 Zhao, Y., Saunois, M., Bousquet, P., Lin, X., Berchet, A., Hegglin, M. I., Canadell, J. G., Jackson, R. B.,
1322 Deushi, M., Jöckel, P., Kinnison, D., Kirner, O., Strode, S., Tilmes, S., Dlugokencky, E. J., and Zheng,
1323 B.: On the role of trend and variability in the hydroxyl radical (OH) in the global methane budget,
1324 *Atmos. Chem. Phys.*, 20, 13011–13022, <https://doi.org/10.5194/acp-20-13011-2020>, 2020.

1325 Zheng, B., Chevallier, F., Yin, Y., Ciais, P., Fortems-Cheiney, A., Deeter, M. N., Parker, R. J., Wang, Y.,
1326 Worden, H. M., and Zhao, Y.: Global atmospheric carbon monoxide budget 2000–2017 inferred from
1327 multi-species atmospheric inversions, *Earth Syst. Sci. Data.*, 11, 1411–1436,
1328 <https://doi.org/10.5194/essd-11-1411-2019>, 2019.

1329 Zhu, L., Mickley, L. J., Jacob, D. J., Marais, E. A., Sheng, J., Hu, L., Abad, G. G., and Chance, K.: Long-term
1330 (2005–2014) trends in formaldehyde (HCHO) columns across North America as seen by the OMI
1331 satellite instrument: Evidence of changing emissions of volatile organic compounds, *Geophys. Res.
1332 Lett.*, 44, 7079–7086, <https://doi.org/10.1002/2017GL073859>, 2017.

1333 Zhu, Q., Laughner, J. L., and Cohen, R. C.: Combining Machine Learning and Satellite Observations to Predict
1334 Spatial and Temporal Variation of near Surface OH in North American Cities, *Environ. Sci. Technol.*,
1335 56, 7362–7371, <https://doi.org/10.1021/acs.est.1c05636>, 2022.

1336 Ziemke, J. R., OMI/MLS tropospheric ozone columns, Greenbelt, MD, USA, Accessed: May 2023,
1337 https://acd-ext.gsfc.nasa.gov/Data_services/cloud_slice/data/tco_omimls.nc